Heteroepitaxial growth of cadmium carbonate at dolomite and calcite surfaces: Mechanisms and rates

Erika Blanca R. Callagon[1†], Sang Soo Lee[2], Peter J. Eng[3], Nouamane Laanait[4], Neil C.Sturchio[5], Kathryn L. Nagy[1], and Paul Fenter[2*]

[1]Department of Earth and Environmental Sciences, University of Illinois at Chicago, Chicago, IL 60607

[2]Chemical Sciences and Engineering Division, Argonne National Laboratory, Argonne, IL 60439

[3]Center for Advanced Radiation Sources, University of Chicago, Chicago, IL 60637

[4]Center for Nanophase Materials Sciences, Oak Ridge National Laboratory, Oak Ridge, TN 37831

[5]Department of Geological Sciences, University of Delaware, Newark, DE 19716

[†]Present address: Department of Civil and Environmental Engineering, University of California, Los Angeles, Los Angeles, CA 90095.

* Corresponding Author: email: fenter@anl.gov

Abstract

The systematic variation of rates and the mechanism of cadmium uptake on the (104) surface of dolomite ($CaMg(CO_3)_2$) were investigated using *in situ* and *ex situ* atomic force microscopy (AFM), *ex situ* specular X-ray reflectivity (XR), and *ex situ* X-ray fluorescence (XRF). Selected experiments were performed on the calcite ($CaCO_3$) (104) surface for comparison. Aqueous solutions of $CdCl_2$, $CaCl_2$, and $NaHCO_3$, undersaturated with respect to calcite and supersaturated with respect to otavite ($CdCO_3$) and the $(Cd_x,Ca_{1-x})CO_3$ solid solution, were reacted with dolomite surfaces for minutes to days. Calcite substrates were reacted with solutions containing 1 to 50 μM $CdCl_2$, and with no added Ca or CO_3. Thin carbonate films following the Stranski-Krastanov growth mode were observed on both substrates. Specular XR and XRF revealed the formation of nm-thick Cd-rich carbonate films that were structurally ordered with respect to the dolomite (104)

The submitted manuscript has been created by UChicago Argonne, LLC, Operator of Argonne National Laboratory ("Argonne"). Argonne, a U.S. Department of Energy Office of Science laboratory, is operated under Contract No. DE-AC02-06CH11357. The U.S. Government retains for itself, and others acting on its behalf, a paid-up nonexclusive, irrevocable worldwide license in said article to reproduce, prepare derivative works, distribute copies to the public, and perform publicly and display publicly, by or on behalf of the Government.

plane. Epitaxial films adopted the calcite crystal structure with a d_{104}-spacing (3.00 Å) intermediate between those of pure calcite (3.04 Å) and otavite (2.95 Å) indicating either a solid solution with $x \approx 0.5$, or a strained Cd-rich carbonate with a composition near that of otavite. The growth rate r of this phase increases with the initial supersaturation of the solution with respect to the solid solution, β_{max}, and follows the empirical relationship, as determined from XRF measurements, given by:

$$r = 10^{-4.88\pm0.42}\left({\beta_{max}}^{2.29\pm0.24} - 1\right), \text{(in units of atoms of Cd/Å}^2\text{/h).}$$

The morphology of the overgrowth also varied with β_{max}, as exemplified by AFM observations. Growth at step edges occurred over the entire β_{max} range considered, and additional growth features including 3 Å high monolayer islands and ~25 Å high tall islands were observed when $\log \beta_{max} > 1$. On calcite, *in situ* XR indicated that this phase is similar to the Cd-rich overgrowth formed on dolomite and images obtained from X-ray reflection interface microscopy (XRIM) reveal the existence of laterally variable Cd-rich domains.

1. Introduction

Cadmium (Cd) is a heavy metal that poses a threat to human health and the environment (e.g., IPCS, 1992; IARC, 1993; Godt et al., 2006, and references therein; OEHHA, 2007; WHO, 2010). Cadmium released to the environment through natural (e.g., volcanic eruptions) and human (e.g., mining and smelting Zn, Cu, and Fe ores, tobacco smoking, fossil fuel combustion, incineration of Cd-containing waste such as Ni-Cd batteries, use of phosphate fertilizers, and recycling of Cd-plated steel and electronic waste) activities can be widely dispersed via deposition onto the ground and transport through the subsurface (ATSDR, 1997; WHO, 2010; NIOSH, 2012). The recommended Cd concentration limit in drinking water is 0.003 mg/L (WHO, 2010). However,

mining operations can contaminate local water supplies, and significantly increase the levels of Cd in groundwater. For instance, stream waters in heavily contaminated areas can contain 0.22 mg/L Cd (Lee et al., 2005).

Metals can be sequestered from aqueous solutions by reactions with mineral surfaces, effectively controlling their transport in surface and ground waters. Methods that have been applied to remove Cd include precipitation as insoluble $Cd(OH)_2$, adsorption with synthetic and natural oxide and hydroxide minerals, and biosorption with agro-industrial waste materials (Rao et al., 2010). Carbonate minerals also have the ability to sequester Cd. Treating contaminated soil with dolomite can reduce plant Cd concentrations (Rochayati et al., 2010) and plant-available Cd (Vondrackova et al., 2013), and calcareous powders have been effective in removing Cd from solution (e.g., McBride, 1980; Davis et al., 1987; Papadopoulos and Rowell, 1988; Zachara et al., 1991; van der Weijden et al., 1994; Martin-Garin et al., 2003; Kohler et al., 2006; Kocaoba, 2007; Yavuz et al., 2007; Ahmed et al., 2009; Mohammadi et al., 2013).

Because of the strong tendency of Cd to partition into calcite, sequestration of Cd by formation of carbonate solid solution will always occur in the presence of calcite, even at trace amounts of aqueous Cd (Tesoriero and Pankow, 1996). Previous high-resolution studies of Cd uptake on single-crystal calcite have shown that the metal is captured at advancing steps or kink sites during growth of calcite or as surface precipitates (Stipp et al., 1992; Reeder, 1996; Chiarello and Sturchio, 1994; Chiarello et al., 1997; Hay et al., 2003; Prieto et al., 2003; Chada et al., 2005; Astilleros et al., 2006; Perez-Garrido et al., 2007; Cubillas and Higgins, 2009; Xu et al., 2014). This uptake, referred to as “incorporation”, can occur by multiple growth mechanisms as a function of solution saturation state. Mechanisms observed by atomic force microscopy (AFM) include nucleation and growth of monolayer and 3D (“tall”) islands, as well as step advance and layer-by-

layer growth. In these studies, rapid dissolution dynamics of the highly soluble calcite surface in water caused significant changes in interfacial chemistry in real time that were not quantified directly. Because of these complexities, examination of Cd uptake over a wide range of solution compositions is challenging, and the effect of composition on growth mechanism has not been fully understood. Furthermore, the extent and rates of Cd uptake and the composition and structure of the phase in which the metal is incorporated remain poorly understood.

In this work, the uptake of Cd on the (104) surface of dolomite ($CaMg(CO_3)_2$) and calcite ($CaCO_3$) was investigated experimentally with a suite of high-resolution measurements including synchrotron X-ray reflectivity (XR), X-ray fluorescence (XRF), X-ray reflection interface microscopy (XRIM), and AFM. Dolomite and calcite are two of the most common carbonate minerals on Earth's surface, both having rhombohedral structures and perfect cleavages in the (104) direction. We have chosen to use dolomite for many of our measurements because its dissolution rate in water at pH 7 and 25 °C is about one order of magnitude lower than that of calcite (approximately 10^{-10} and 10^{-11} mol/cm^2/s, respectively) (Chou et al., 1989; Morse and Arvidson, 2002). Consequently, the saturation state of otavite in the reaction solution can be controlled with smaller perturbations of the substrate topography (e.g., through dissolution) and use of higher Cd concentrations which simplifies the experimental design. By characterizing the structure, composition, and surface distribution of the Cd-rich overgrowth, relationships were determined between the initial saturation state of the solution and the morphologies and growth rates of the overgrowth phase. Finally, our results are compared to previous and current findings on calcite in order to gain insight into the effects of substrate lattice mismatch on growth.

2. Experimental Details

2.1 Sample preparation and experimental conditions

Optically clear dolomite (Brazil) and calcite (Brazil, Bolivia) crystals were used in the experiments. Each crystal rhomb was first cut into the shape of a bar using a low-speed diamond saw with four sides perpendicular to the (104) plane. Immediately prior to each experiment, the end of the bar was lightly tapped on the edge with a razor blade until a thin chip with a fresh surface (with dimensions 5 – 10 mm × 5 – 10 mm × 1 – 2 mm) free of visible steps was obtained.

For dolomite surfaces, reaction solutions were prepared by dissolving ACS reagent grade $CdCl_2$, $CaCl_2$, and $NaHCO_3$ salts in deionized water (DIW), or by mixing aliquots of concentrated aqueous solutions of $CdCl_2$, $CaCl_2$, and $NaHCO_3$ in DIW. The $NaHCO_3$ (salt or aliquot of a concentrated solution) was added a few seconds to a few minutes before the dolomite sample to minimize the homogeneous precipitation of Cd-carbonate phases. In the following text, the nomenclature [Cd], [Ca], etc., refers to total species concentrations, and respective charges are shown when referring to specific ionic Cd^{2+} or Ca^{2+} species. Solution compositions were varied to test the effect of [Cd], saturation state, and [Cd] to [Ca] ratios on growth. Cadmium concentrations ranged from 0.001 to 0.5 mM, whereas [Ca] and [CO_3] ranged from 0.1 to 1 mM. In most experiments, [Ca] and [CO_3] were equal, and [Cd] was varied. In other experiments, [Cd] was held constant, and [CO_3] and [Ca] were equal and varied together. Finally, in a few experiments, the [Cd]/[Ca] ratio was varied while the sum of [Cd] and [Ca] was maintained equal to 1 mM, and [CO_3] was 0.2 mM. Solution speciation and saturation states of the various phases were calculated with PHREEQC (Parkhurst and Appelo, 2011) using the MINTEQ.v4 database. Saturation indices for calcite and otavite were calculated for the reactions:

$$SI\ CaCO_3 = \log \frac{a_{Ca^{2+}}\, a_{CO_3^{2-}}}{K_{sp,CaCO_3}} \text{ and} \quad (1)$$

$$SI\ CdCO_3 = \log \frac{a_{Cd^{2+}}\, a_{CO_3^{2-}}}{K_{sp,CdCO_3}}, \quad (2)$$

where a is the activity of the Ca^{2+}, Cd^{2+}, or CO_3^{2-} ion, $\log K_{sp,CaCO_3}$= -8.48, and $\log K_{sp,CdCO_3}$= -12.0. In the simulations, the solutions were equilibrated with atmospheric CO_2 ($pCO_2 = 10^{-3.4}$ atm).

The formation of a Cd-rich $(Cd_x,Ca_{1-x})CO_3$ solid solution is expected based on the Lippmann (Fig. EA1) and Gibbs free energy of mixing (Fig. EA2) diagrams. We consider the nucleation and growth of the $(Cd_x,Ca_{1-x})CO_3$ solid solution, with supersaturation, β, defined as:

$$\beta = \frac{a(Cd^{+2})^x a(Ca^{+2})^{1-x} a(CO_3{}^{-2})}{\left(K_{CaCO_3}(1-x)\right)^{1-x} (K_{CdCO_3}x)^x}, \quad (3)$$

where a, K, and x are the activities of the constituent ions, solubility product constants, and mole fractions of the ions in the solid solution, respectively (Fig. EA3) (Prieto et al., 1993; Prieto, 2009). The maximum of the curve, β_{max}, defines the composition, i.e., mole fraction of Cd, of the solid solution phase at which the aqueous solution is most supersaturated thermodynamically. For each solution, the composition and degree of supersaturation of the most stable $(Cd_xCa_{1-x})CO_3$ solid solution were calculated following Eq. 3 (Fig. EA3). The calculations show that the AFM, XR and XRF experimental solutions (Tables 1 and 2, respectively) were supersaturated with respect to otavite and the Cd-carbonate solid solution in most cases, and undersaturated with respect to dolomite and calcite. The solutions were undersaturated in all other solid phases (Table EA1).

Reaction times were varied depending on the supersaturation of the solid solution, β_{max} (Tables 1 and 2). In general, a shorter reaction time (few minutes to few hours) was employed for solutions with high β_{max}, whereas a longer duration (hours to few days) was used for solutions with low β_{max}. We also varied reaction times for the same initial chemical conditions to evaluate

potential effects on the growth rate caused by the changing saturation state of the solution with time.

Experiments were carried out at ambient temperature. Solution pH was not separately controlled. The calculated pH values were generally between 7 and 8 (Tables 1 and 2), and were in good agreement with measured pH values. Cadmium concentrations of selected reaction solutions were verified with Inductively Coupled Plasma – Optical Emission Spectrometry (ICP-OES).

Reaction solutions for the calcite experiments were prepared by mixing ACS reagent grade $CdCl_2$ salt with DIW that was previously equilibrated with atmospheric CO_2, as in Perez-Garrido et al. (2007) (Table 3). The solutions used for the calcite experiments did not have added Ca or CO_3, and were undersaturated with respect to otavite (Table EA2). A separate set of calcite experiments was carried out adopting the procedure of Xu et al. (2014), wherein a small amount of a concentrated $CdCl_2$ solution was added to calcite-reacted DIW (Table 4).

2.2 Atomic Force Microscopy (AFM)

An Asylum Research MFP-3D Stand Alone AFM was operated in AC mode using Si_3N_4 probes (nominal spring constant, 0.1 N/m; nominal resonant frequency, 19 kHz; Bruker) for measurements in solution, and using rectangular Si probes (Asylum Research) for imaging in air. Image processing was limited to second-order background subtraction (‘flattening’).

2.2.1 *In situ* AFM

A sample was placed in a container with DIW within seconds of cleaving, and then mounted on the fluid cell base with marine epoxy. The sealed cell (~2.5 mL in volume) was filled within

minutes with DIW. The scan rate was set between 1 to 1.5 Hz. Collecting a 5 μm × 5 μm image took about 4 minutes to complete at a 1 Hz scan rate and 256 points per line. The sample was imaged first in DIW, and the AFM operation parameters were optimized for fluid imaging. For dolomite, which has a slow dissolution rate, the solution in the fluid cell was exchanged by manually injecting a volume of the Cd-containing solution of about 5 times the cell volume, corresponding to at least 12 mL. For calcite, which dissolves much faster than dolomite, at least 12 mL DIW was flushed through the fluid cell immediately before injecting at least 12 mL of $CdCl_2$ solution. This minimized residual Ca and CO_3 in the fluid cell that could react with the Cd-containing solution, and ensured that the dissolution of calcite after addition of the $CdCl_2$ solution would account for most of the Ca and CO_3 participating in the Cd uptake. Also, a complete solution exchange was desired to avoid instantaneous supersaturation of the solution and precipitation in solution caused by any CO_3 already present in the fluid cell before addition of $CdCl_2$ solution. For both substrates, the flow was stopped after the solution exchange and then a series of images was collected periodically for up to 6 hours. Multiple areas in the sample were imaged for each experiment.

2.2.2 *Ex situ* AFM

The dolomite sample was briefly rinsed with DIW to remove fine mineral particles that may have resulted from the cleaving process, and within three seconds was placed in a centrifuge tube containing 30 mL of Cd-containing reaction solution. The tube was placed on a shaker table for the duration of the reaction and until immediately before drying. This procedure was also employed for the *ex situ* calcite experiments that simulated those of Perez-Garrido et al. (2007).

The Cd-reacted dolomite or calcite was dried with a brief jet of nitrogen gas and placed on top of a glass slide without using adhesive.

For both *in situ* and *ex situ* AFM experiments, height and phase images were collected. Phase contrast in the AFM images may result from differences in tip-sample interactions caused by compositional inhomogeneity in the sample (e.g., otavite has a larger bulk modulus than calcite (97 GPa vs. 76 GPa) (Zhang and Reeder, 1999)). Phase contrast between calcite and Cd-rich overgrowth in lateral force microscopy images has been demonstrated previously (Hay et al., 2003; Cubillas and Higgins, 2009; Xu et al., 2014). The variations in the settings used during the operation of the AFM produced differences in absolute values in phase for images of the same sample and among different samples. Values of the phase shifts change with driving amplitude and ratio between driving and setpoint amplitudes, which can be explained in part by effects of tip-sample interactions on cantilever properties (Bar et al., 1997). Nevertheless, the distinct phase contrast was present in all cases, and allowed differentiation of the substrate and the growing Cd-carbonate phase. All phase images are presented in grayscale.

2.3 Specular X-ray Reflectivity (XR), X-ray Fluorescence (XRF), and X-ray Reflection Interface Microscopy (XRIM)

X-ray Reflectivity (XR) is sensitive to surface and interface structures, and provides high-resolution and quantitative chemical and structural information valuable for studying film growth. Specular XR is sensitive to the structure normal to the scattering plane, which in this case is the mineral surface. Experimental XR measurement methods were similar to those described previously (e.g., Fenter, 2002; Fenter et al., 2003; Callagon et al., 2014), and were performed at Sectors 13-BMC, 13-IDC, and 33-IDD of the Advanced Photon Source (APS). Specular XR

measurements were carried out at photon energies of 14 keV (33-IDD), 14.9 keV (13-BMC), and 16 keV (13-IDC) corresponding to X-ray wavelengths, λ, of 0.886 Å, 0.832 Å, and 0.775 Å, respectively. X-ray reflectivity is measured as a function of momentum transfer, Q, defined as $Q = (4\pi/\lambda) sin\,(2\theta/2)$, where 2θ is the scattering angle. Reflectivity is given by: $R(Q) = (4\pi r_e/QA_{UC})^2 |F_{UC}F_{CTR} + F_{int} + F_W|^2$, where $r_e = 2.818 \times 10^{-5}$Å is the classical electron radius, A_{UC} is the area of the unit cell, and F is the structure factor of the bulk unit cell (*UC*), interfacial region (*int*), or water (*W*). The structure factor, F, is defined as $F = \sum_j f_j\,(Q) \exp(iQz_j) \exp\left[-\frac{1}{2}(Qu_j)^2\right]$, where f_j, z_j, and u_j are the atomic scattering factor, position, and vibrational amplitude of atom j. The reflectivity, which was measured from Q ~ 0.2 – 5.0 Å^{-1}, is in the form of a crystal truncation rod (CTR) (Robinson, 1986; Fenter, 2002). A CTR is a weak rod of reflected intensity oriented normal to the surface, and connects Bragg peaks along the specular rod in reciprocal space. Bragg peaks along the specular CTR are located at $Q = n2\pi/d$, where n is an integer, and d is the lattice spacing in the surface normal direction. Dolomite, calcite, and otavite have d_{104} spacings of 2.884 Å, 3.0355 Å, and 2.95 Å, respectively, leading to first- and second-order Bragg reflections at Q = 2.179 Å^{-1} and 4.357 Å^{-1} for dolomite, Q = 2.070 Å^{-1} and 4.140 Å^{-1} for calcite, and Q = 2.130 Å^{-1} and 4.260 Å^{-1} for otavite. The X-ray data were collected using a PILATUS area detector, enabling fast data acquisition.

We obtained XR data for several dolomite samples (Table 2). The dried sample was mounted on aluminum or brass posts for X-ray characterization in air or a helium gas environment. The samples exhibited heterogeneous topography, e.g., differences in the vertical surface roughness and the lateral surface step density. Specular XR was collected from 1 to 3 different areas on each sample surface to investigate the effect of step density on Cd uptake. We estimated the average surface step spacing (i.e., domain size) by measuring the width of the reflection at Q ~ 1.2 Å^{-1} from

the PILATUS images (Robinson, 1986). The largest domain size that can be measured is limited by the detector resolution in pixels, and is ~6 μm. Details of the domain size analysis are given in the Electronic Annex.

The amounts of Cd on the surface were derived by quantitatively comparing the CTR data with calculations of the reflectivity derived from atomistic models of the surface and overgrowth film. Following the thermodynamic calculations that indicated a Cd-rich carbonate phase, the overgrowth was assumed to be a $CdCO_3$ film. As will be described below, the XR results reveal that growth was in the form of an epitaxial thin film registered to the substrate lattice. The structure of this epitaxial otavite film was described by using a simplified model characterized by a lattice spacing, a coverage, and a film roughness. This model can reproduce the XR signal at the film Bragg peak without the need to include additional structural details (such as a variation of the film lattice spacing with height). Within this model, the variation in Cd coverage or occupancy, θ_i, in the film as a function of height was modeled as an error function profile given by:

$$\theta_n = \varphi \, \frac{1}{2}\left[1 - \mathrm{erf}\left(\frac{z_n - z_0}{\sqrt{2}\,|w_0|}\right)\right], \qquad (4)$$

where the parameter z_0 and w_0 are the inflection point and rms width of the error function (erf) that are used to model the distribution of heights of the film surface, and z_n is the height of a given layer, n. The pre-factor, φ, is the theoretical coverage of otavite per unit cell area (A_{uc} = 18.54255 Å^2) of dolomite when $z_n \ll z_0$, which was assumed not to exceed 1. The height of each otavite layer was calculated as $z_n = \Delta + n(d_{104})$, where d_{104} is the film vertical layer spacing and Δ is the film-substrate separation, i.e., distance between the substrate surface plane and the first layer of the film. The average thickness of the film, $\langle z \rangle$, is given by $\langle z \rangle = d_{104} \frac{\sum \theta_n z_n}{\sum \theta_n}$. The decrease in film layer coverage with distance from the dolomite surface is supported by AFM findings, which will be described in more detail below. Details of the modeling procedure are given in the Electronic

Annex (Figs. EA4 and EA5). The Cd occupancy of each layer, θ_i, ranges from 0 to 1 ML (1 monolayer, ML = 1 Cd/A_{uc}). The CO_3 anion groups in the (104) lattice planes are tilted by 43.894° and 43.612° from the surface normal direction for dolomite and otavite, respectively.

From comparison between the measured and calculated XR data, the film thickness and roughness, film-substrate separation, and film lattice spacing along the (104) direction can be determined from each CTR. Model calculations illustrate how the CTR shape is highly sensitive to the thickness and distribution of the film (Fig. 1). Briefly, a CTR resulting from a smooth thin film (e.g., 2 full layers) can be characterized by oscillations in the reflected intensity and the presence of broad film Bragg peaks (Fig. 1A). On the other hand, a CTR of a rough thick film (e.g., ~9 partial layers) exhibits distinct film Bragg peaks (black arrows) at Q values corresponding to the film d-spacings (Fig. 1B).

For selected dolomite samples, XRF measurements of Cd were collected at a beam energy of 28.6 keV (13-BMC). We quantified total Cd on the surface from the integrated signal around the Cd K-α emission line (23.2 keV), using a strontium standard for calibration to determine absolute Cd atomic densities. Additional CTRs were collected at the same sample areas and with the same beam configuration to compare amounts of Cd from XR analysis to those obtained from XRF. Reflectivity-derived Cd coverages quantified the fraction of the overgrowth that was ordered and coherently oriented with the substrate, whereas those derived from fluorescence measurements included all Cd on the surface, irrespective of its structure or orientation.

Analysis of the reflectivity data focused on the data near either the (104) or (208) film Bragg peaks, at Q values from about 1.5 to 2.5 $Å^{-1}$ and from 3.5 to 4.6 $Å^{-1}$, respectively. These regions are sensitive to the thickness and coverage of the $CdCO_3$ film, and are relatively insensitive to the finer-scale structure of the substrate-film interface. For CTR measurements at 14 and 14.9 keV,

best-fit models were obtained typically from the data around the (208) film Bragg peaks where the film and substrate Bragg peak positions are better separated in Q. For CTR measurements at 28.6 keV and for samples with low Cd occupancies, the analysis was performed at the first-order Bragg region. The quality of fit was quantified by χ^2 and R-factor, given by the following equations: $\chi^2 = (1/N)\sum_i\left[\left(I_i - I_{i,calc}\right)/\sigma_i\right]^2$ and $R = (1/N)\sum_i\left|\left(I_i - I_{i,calc}\right)/I_i\right|$, where N is the number of data points, and I_i, $I_{i,calc}$, and σ_i are the measured intensity, calculated intensity, and measured uncertainty of the ith data point.

We also obtained *in situ* XR data (33-IDD) for a calcite crystal that was reacted for 23 hours in 10 μM $CdCl_2$ solution, and then placed in a thin film cell filled with the same reacted 10 μM $CdCl_2$ solution shortly before the measurements. The top six layers of the surface and one adsorbed layer were included in the analysis of the CTR of the reacted calcite. The positions of Ca and CO_3 were allowed to vary, as well as the rotations of the CO_3 group with respect to the surface normal direction. In the model, Cd ions substitute for Ca in calcite, which was defined as having a unit cell area, A_{uc} = 20.1982 Å^2 and CO_3 rotation of 44.621°.

Images of a Cd-reacted calcite surface were also obtained with X-ray reflection interface microscopy (XRIM), which is a full-field imaging technique that images the lateral variation of the reflectivity signal through scattering contrast from the reacted surface (Fenter et al., 2006; Fenter et al., 2010; Laanait et al., 2014; Laanait et al., 2015), essentially a spatially resolved version of XR. The XRIM images, obtained at a scattering condition, Q = 2.29 Å^{-1}, close to that of the otavite (104) thin-film Bragg peak, contain information about the interfacial structure as in X-ray reflectivity (e.g., composition), and are also sensitive to topography (e.g., presence of monolayer steps) (Fenter et al., 2006; Fenter et al., 2010). In particular, regions with higher signal will be associated with local domains with higher Cd concentration.

3. Results

3.1 Atomic force microscopy observations of the growth process

3.1.1 Dolomite

Multiple growth morphologies were observed on dolomite that mainly depended on the initial saturation state of the reaction solution, β_{max}, with respect to the Cd-carbonate solid solution. At low supersaturation (log $\beta_{max} \leq 1.0$), growth occurred as monolayers 3 Å in height that originated at step edges (Fig. 2). Initial reaction with DIW resulted in some dissolution of dolomite as evident from surface pitting, and phase images of the initial dolomite surface showed uniform contrast except at steps (Fig. 2A). Upon reaction, distinct phase contrast was observed between the overgrowth and the substrate. The absolute shifts in phase varied among the different images, and the overgrowth and substrate are represented in bright and dark gray, respectively, for consistency. Growth ensued only at specific orientations of step edges (solid red lines), but not at others (dashed yellow lines). Monolayer growth continued to dominate after a day of reaction (Fig. 2D).

A more complex morphology was observed at intermediate supersaturation ($1.0 < \log \beta_{max} < 2.0$). Monolayer growth was found at steps along with the formation of monolayer thick (3 Å) and ~2.5 nm tall islands on terraces, designated by red and yellow arrows, respectively (Fig. 3). The monolayer islands are fan-shaped with edges that were initially straight in at least two directions, but with time evolved to become more irregular or scalloped. These overgrowths expanded laterally and coalesced, forming full layers after approximately 1 day (Fig. EA6). For longer-term experiments, we also observed features several nanometers in height (yellow box in Fig. EA6B-C). These thick features have straight edges and were produced by the nucleation and growth of

monolayer islands at the same spots on the surface, resulting in a 'stacked' appearance. These features may be explained by the presence of screw dislocations on the dolomite surface.

Finally, at higher supersaturation (log β_{max} > 2.0), growth was observed at steps as well as by rapid nucleation and expansion of fan-shaped monolayer islands (Fig. 4). The surface was nearly covered with the overgrowth in about 15 minutes (Fig. 4C). Selected *ex situ* AFM images at high supersaturations demonstrate the effect of heterogeneity in surface roughness on coverage of the overgrowth (Fig. 5), in which a high surface step density facilitated film growth compared to smoother surfaces (Fig. 5A vs. Fig. 5B).

A summary of the AFM observations at different experimental conditions illustrates the three regimes of overgrowth morphology: (1) growth at step edges; (2) growth at step edges and formation of monolayer islands; and (3) growth at step edges, and formation of monolayer and tall islands (Fig. 6). The monolayer islands grew to thicker features composed of multilayers with increasing reaction time and supersaturation. The morphologies are controlled by the initial supersaturation of the solution and the relative concentrations of Cd, Ca, and CO_3.

3.1.2 Calcite

In situ AFM on calcite reacted with 50 µM $CdCl_2$ solution revealed growth originating at steps, which was followed by the formation of fan-shaped 3 Å high islands on the overgrowth (Figs. 7 and EA7). Initially upon addition of the $CdCl_2$ solution, dissolution occurred as evidenced by the appearance of elongated pits on the surface (Fig. EA7B). This departure from the typical rhombohedral shape has been previously observed in calcite etch pits in the presence of Cd (Perez-Garrido et al., 2007; Xu et al., 2014; Xu et al., 2015). The dissolution of calcite was the only source of dissolved CO_3 which was required for precipitation of the Cd-carbonate phase. The phase

contrast between the substrate (dark gray) and the overgrowth (bright gray) was evident in the calcite experiments as well (Figs. 7, EA7D, and EA8). The monolayer islands coalesced to form full overgrowth layers (Fig. 7). Similar results were obtained for samples reacted with 20 to 40 μM [Cd], where target Cd concentrations were attained by addition of concentrated $CdCl_2$ solution in water previously reacted with calcite (Xu et al., 2014) (Fig. EA8). At 1 and 5 μM Cd concentrations, possible minor growth at step edges is seen in phase images (Fig. EA9), in addition to jagged calcite step edges produced by dissolution (Fig. EA7B).

In cases where extensive growth was observed, growth slowed during the course of reaction, and ceased once the surface was covered. We observed similar growth morphologies on calcite when solutions containing $CdCl_2$, $CaCl_2$, and $NaHCO_3$, as in dolomite experiments, were used (results not shown).

3.2 Cd uptake rates on dolomite from X-ray fluorescence

Cd atomic densities on the dolomite surface were measured with XRF over a nearly 10^3-wide range of β_{max} (Table EA3). The amount of Cd in atoms of Cd/Å^2 and rates of Cd uptake in atoms of Cd/Å^2/h on different areas of a single sample varied by as much as a factor of ~16, for example as seen in Experiment XR-13. In the context of the AFM results (Fig. 6), we postulate that this was caused by differences in the surface domain size or average step spacing across the sample, i.e., different areas in heterogeneous surfaces may have had different amounts of overgrowth. To test this idea, the growth rate was normalized by multiplying the growth rate by the surface domain size that was directly measured using XR (Table EA4; Fig. EA10) on the same area where the XRF measurements were collected. This normalization defines the growth rate in units of Cd/Å/h (Table EA3) that is appropriate for growth from steps. Ideally, the total Cd occupancies for

different areas within a sample should be equal or similar after normalization to step spacing. Further, an average step advance rate due to film growth can be estimated using growth rates from XRF or XR by multiplying the rate with the molar volume of the crystal, and then dividing by the step height and step density. The calculated step velocities are comparable to those measured from AFM.

In the case of Experiment XR-13, the step spacing-normalized Cd growth rates have a much smaller range of values (factor of ~1.6) than the unadjusted range of growth rates on different parts of the sample (factor of ~16), confirming that a primary control over the local surface Cd coverage was the surface topography, e.g., step density (Table EA3). However, this normalization procedure did not explain the differences in the amounts of Cd deposited within a single sample for all cases. This normalization procedure is expected to work only where the surface roughness is directly resolved by the XR measurement, as seen by a finite broadening of the surface truncation rod at the anti-Bragg condition. This condition will not be satisfied if the surface steps are oriented in a direction approximately parallel to the X-ray scattering plane. The orientation of the steps in the sample in relation to the X-ray beam was not separately controlled in our measurements. Consequently, this procedure was not always useful as a way of quantifying the relative Cd coverages. For samples having randomly oriented steps with sub-micron step spacings, the orientation of the sample relative to the beam would have had less effect on the measured domain sizes.

The uptake rates obtained from XRF were fitted to an affinity-based kinetic model (e.g., Nancollas and Reddy, 1971; Aagaard and Helgeson, 1982; Inskeep and Bloom, 1985; Lasaga et al., 1994) for mineral growth having the following general functional form:

$$r = k\left(e^{\frac{n\Delta G}{RT}} - 1\right), \quad (5)$$

where r is either the net growth rate (in units of Cd/Å^2/h) or the step-spacing normalized rate (in units of Cd/Å/h), k is the rate coefficient (h^{-1}), n is an empirical constant, R is the molar gas constant, T is the temperature, and ΔG is the change in Gibbs free energy of the reaction $Cd_xCa_{1-x}CO_3 = xCd^{2+} + (1-x)Ca^{2+} + CO_3^{2-}$, which is related to the saturation state of the solution by:

$$e^{\frac{\Delta G}{RT}} = \beta_{max}. \quad (6)$$

Values of k and n were obtained by least squares fitting of the data to:

$$r = k({\beta_{max}}^n - 1). \quad (7)$$

The following relationships were obtained:

$$r = 10^{-4.88\pm0.42}\left({\beta_{max}}^{2.29\pm0.24} - 1\right) \quad (8)$$

for the rate per area (in units of Cd/Å^2/h) (Fig. 8A) and

$$r = 10^{0.83\pm0.19}\left({\beta_{max}}^{1.43\pm0.12} - 1\right) \quad (9)$$

for the normalized rate (in units of Cd/Å/h) (Fig. 8B). This normalized rate corresponds to the linear growth rate of the otavite phase from a single step.

3.3 Cd uptake rates and overgrowth structure from specular X-ray reflectivity

3.3.1 Dolomite

X-ray reflectivity data (Fig. 9) revealed the development of film Bragg peaks indicating the formation of a phase that was structurally ordered with respect to the dolomite (104) surface plane. The fitting parameters according to Eq. 4 corresponding to the best-fit structure for all of the samples are given in Table EA5. The overgrowth Bragg peaks were observed at $Q \sim 2.1$ Å^{-1} and

4.2 $Å^{-1}$, which are lower than Q corresponding to dolomite Bragg peaks and indicate that the overgrowth phase had a vertical layer spacing larger than that of dolomite. The electron density profiles and Cd occupancies derived from the best-fit structure for selected CTRs in Fig. 9 are shown in Fig. 10.

The average film lattice spacing, d_{104}, was determined to be 3.00 $\pm$ 0.01 Å (Fig. 11; Table EA5). This parameter was fixed to 3.0 Å in CTRs with film Bragg peaks that were not pronounced or well-defined from the data, e.g., when surface total Cd occupancies were < ~1.5 ML. This overgrowth lattice spacing was larger than those of dolomite (2.884 Å) and otavite (2.95 Å), and smaller than that of calcite (3.0355 Å). This nominally implies an overgrowth composition of approximately $Cd_{0.5}Ca_{0.5}CO_3$ based on the relative d_{104} of the solid solution end-members calcite and otavite. This composition, however, is inconsistent with thermodynamic predictions, as discussed below.

Cadmium coverages on reacted dolomite surfaces were obtained from analysis of the XR data (Table EA6). Total Cd occupancies ranged from ~ 0.1 to 20 ML typically, which is equivalent to ~0.005 to ~1 Cd/$Å^2$. Growth rates were obtained from the XR data, and are related to the initial solution β_{max}, as for the XRF data (Fig. 12). Samples reacted with solutions having $\beta_{max} < 1$ or $\beta_{max} > 150$ were not included in the growth rate analysis (Fig. 12). At low β_{max}, the growth rate was extremely slow and Cd coverages were consequently low; the lack of a pronounced Bragg peak for the overgrowth increased the uncertainty of the modeled Cd occupancy. The specular XR signal was sensitive to the part of the film that was coherent with the substrate in the surface normal direction. At extremely high β_{max} where Cd coverages tended to be greater, the development of an incoherent film, e.g., with tilted domains caused by strain-driven dislocations, became more

significant, resulting in an underestimation of total Cd occupancy on the surface. This may also be true for moderate β_{max} experiments with longer durations.

The growth rate increased with initial solution supersaturation as was shown by the XRF measurements (Table EA6; Fig. 12). In some cases, the normalization to the substrate domain size or step spacing resulted in a smaller spread in growth rates measured in one sample. This is evident for Experiments XR-6, XR-11, and XR-13, where the ratios of the maximum and minimum rates in the different areas of the samples were 3.3, 8.4, and 18.5 initially, and then became 1.1, 1.5, and 3.4, respectively, after dividing the nominal rates by the step density. However, in most cases, the normalization to step spacing resulted in a larger divergence in values of growth rates within a sample (Fig. 12B). When Eq. 7 is fit to the rate per area (Cd/Å^2/h) (Fig. 12A), the relationship is

$$r = 10^{-4.64\pm0.13}\left(\beta_{max}{}^{1.77\pm0.08} - 1\right) \quad (10)$$

When fit to the rate normalized to the surface step spacing (Cd/Å/h) (Fig. 12B), we obtained:

$$r = 10^{-0.98\pm0.14}\left(\beta_{max}{}^{2.01\pm0.09} - 1\right) \quad (11)$$

We further evaluated the variation in growth rate obtained at one initial value of $\log \beta_{max}$ (~1.5) by analyzing a subset of data with the same initial solution but different reaction times (boxed data points in Fig. 12). Samples XR-16, XR-17, XR-18, XR-19, and XR-20 were all reacted with [Cd] = [Ca] = [CO_3] ~ 0.2 mM (Table 2). Reaction times were 4, 12, 12.07, 24, and 46.50 hours, respectively. Both the growth rate and step spacing-normalized growth rate showed a slight decrease with reaction time, although R^2 values indicate that this relationship is statistically weak (Fig. EA11).

The comparison of Cd coverages as measured by XRF and XR provides additional insights. Cadmium coverages from XRF corresponded well to those from XR for coverages less than 0.4 Cd/Å^2 or ~6 ML (Table EA7, Fig. 13), but were consistently higher than those from XR by a factor

of about 1.4 for coverages > 0.4 Cd/Å^2 (solid line in Fig. 13). We observed evidence from non-specular X-ray reflectivity scans of "powder-like" otavite that was oriented in various directions (Fig. EA12). This phase was not quantified in the specular XR, and may explain the consistently higher Cd densities from XRF. At high Cd coverages where the fraction of the incoherent film became more significant, there was a weaker relationship between Cd occupancies from XRF and those from XR. This suggests a transition in the process of incorporation at Cd occupancies > ~0.4 Cd/Å^2, which is described in more detail below.

3.3.2 Calcite

In order to understand the interaction of calcite surfaces with Cd-containing solutions, X-ray reflectivity data were obtained for a calcite sample reacted with a 10 µM $CdCl_2$ solution. The formation of Cd-rich carbonate film on calcite caused a characteristic increase in the reflected intensity near the otavite thin-film Bragg peak position leading to the formation of a broad Bragg peak (Q = 2.4 Å^{-1}) (Fig. 14A). The electron density profile for the best-fit model revealed the variation of the Cd-containing film structure as a function of depth (Fig. 14C). The average film layer spacing estimated from the positions of the cations in the first to third film layers was 2.96 Å. Our best-fit model showed the incorporation of Cd in the top three layers at the calcite surface (Fig. 14C), with Cd occupancies of 0.45 ± 0.02, 0.27 ± 0.01, and 0.22 ± 0.06 ML, for the first (top), second, and third layers, respectively. The model also indicated a significant displacement towards the substrate for Ca (and Cd) (0.13 ± 0.01 Å) in the layer closest to the mineral-fluid interface. The first (top) and second layer CO_3 anion groups were displaced by 0.42 ± 0.03 Å and 0.22 ± 0.03 Å towards the substrate, respectively, and were rotated 8.16 ± 2.3° and 14.17 ± 1.7°

from the bulk value (44.621°). The positions of Ca and CO_3, and the rotations of CO_3 in the third to sixth layers, did not significantly vary from ideal positions and rotations for bulk calcite.

Further information about the lateral variation of the otavite film structure was obtained from *ex situ* XRIM measurements (Fig. 14B). These results showed regions of higher local reflectivity associated with the formation of Cd-rich domains, because they were taken at conditions close to the Cd film Bragg peak position (Fig. 14B). At this scattering condition, the observed intensity in the XRIM image is proportional to N_O^2, where N_O is the local otavite film thickness (in layers). Consequently, these images showing lines of increased intensity indicated that the otavite film growth nucleated on substrate steps, consistent with the ex-situ AFM observations.

4. Discussion

4.1 Evolution of the reaction solution

The use of the slowly dissolving dolomite substrate allowed for investigation of the growth process over a large range of supersaturations and Cd concentrations, and provided insights into the process of film formation that we otherwise would not have obtained from experiments on calcite alone. As Cd uptake proceeded, the expected evolution of selected initial solutions was assessed by calculating the change in $CdCO_3$ supersaturation as 1×10^{-7} mol of otavite was precipitated from the experimental solution volume of 30 mL (Fig. EA13A). The supersaturation of the solid solution, β_{max}, was similar to that for $CdCO_3$ but slightly higher. The XR and XRF results showed that ~0.1 to 50 ML of $CdCO_3$, equivalent to ~0.5×10^{14} to 3×10^{16} Cd atoms per cm^2 formed on the surface. With a surface area of ~3 cm^2, we estimate that between 2.5×10^{-10} and 1.5×10^{-7} moles of Cd were removed from the solution. This amount of precipitation does not change the $CdCO_3$ saturation index significantly in most experimental conditions, although the

slight decrease in supersaturation may have contributed to the apparent decrease in growth rate with reaction time (Fig. EA11). This apparent decrease may be explained partially by the transition in the Cd incorporation process that was evident in the comparison of XR- and XRF-derived Cd coverages (Fig. 13), in which the total Cd occupancies from XR are found to underestimate the total coverage measured by XRF for Cd coverages greater than ~0.4 Cd/Å^2. We note that the incorporation of Mg in the precipitates was not considered. Because the dissolution of dolomite was slow, we did not expect a significant amount of Mg to have been released into the solution. Also, as growth proceeded, the dolomite substrate became covered with the overgrowth, further inhibiting its dissolution. The dissolution of dolomite may be more important for solutions that have relatively low supersaturations with respect to the Cd-containing precipitates because film growth rates are lower, allowing for the continued exposure of dolomite to the reaction solution. In addition, PHREEQC calculations show that addition of Mg with concentration equal to that of Cd in selected experimental conditions results in undersaturation in Mg-containing phases.

Unlike dolomite, the overgrowth on calcite in our experimental conditions required dissolution of the calcite substrate. The evolution of the reaction solution in the case of a calcite substrate was also calculated (Fig. EA13B). In the calculation, the initial air-equilibrated solution (pH 5.6) contained only $CdCl_2$, and was reacted with calcite that dissolves stoichiometrically in small increments. The solution pH was allowed to evolve in each reaction step. The addition of Ca and CO_3 from dissolving calcite caused a rapid increase in the $CdCO_3$ saturation values and eventual precipitation of the solid solution at SI $CdCO_3$ = 0. The onset of solid solution formation occurred earlier with less calcite dissolution when the initial Cd concentration was higher. A higher initial solution pH would also allow precipitation with less dissolved calcite (not shown). The solution remained undersaturated in both calcite and otavite while the most stable phase, the $Cd_xCa_{1-x}(CO_3)$

solid solution, formed (Fig. EA13B). In all cases, the solid solution phase was Cd-rich (the aqueous phase is Cd-poor), and remained so until aqueous Cd was depleted (not shown). These calculations show the conditions in which the Cd-containing solid solution began to form in the calcite experiments, and give an estimate of how much calcite dissolution was required for precipitation of the overgrowth.

4.2 Controls on the growth process and their limitations

The results discussed above show that the initial value of β_{max} is the predominant control on both the morphology (Fig. 6) and growth rate (Figs. 8 and 12; Eqs. 8 to 11) of the Cd-carbonate overgrowth on dolomite. The empirical coefficient *n* derived from the general model in Eq. 7, having values between 1.4 and 2.3, has been related to the growth mechanism (see e.g., Teng et al., 2000), corresponding to layer by layer and island nucleation growth.

We observed variable growth rates obtained from both XR and XRF for experiments at the same value of β_{max}, indicating that at least one factor besides supersaturation influences Cd uptake. The AFM images reveal that growth initiates at dolomite steps. From our macroscopically averaged results, we also found that local step density is an important factor, with strong variations of the apparent growth rates, even for two regions of a single sample surface. When the step density was probed directly by XR (e.g., through the broadening of the reflected beam), we found that most of the differences in growth rates were removed. An additional factor that controlled this variation appears to be the extent of otavite film growth. As the overgrowth spread, the influence of original substrate step distributions may have been reduced. This was evident in the step spacing-normalized rates from XRF for samples with high solution β_{max} and surface Cd occupancies (Experiments XR-28 and XR-30 in Table EA3), in which the normalization increased

the range of observed rates. Also, growth was rapid at high supersaturations and was dominated by the formation of two-dimensional islands (e.g., Fig. 4), resulting in a less prominent effect of step spacing on growth. From these observations, we conclude that the control over the macroscopically observed growth rates by the local surface step density was most prominent for samples with lower Cd coverages or short reaction times (e.g., Experiment XR-13), when the surface domain size was accurately measured.

A transition in the growth mode as a function of film thickness was evident from a direct comparison of XR and XRF-derived Cd occupancies (Fig. 13). This change in behavior was correlated with a transition in the otavite film structure (Callagon, 2016).

4.3 Comparison of Cd incorporation in dolomite and calcite and the effect of misfit

Much of the previous work on Cd incorporation on carbonate was performed on calcite. Our investigation instead used dolomite as a substrate, which allowed us to systematically control the composition and saturation state of our reaction solutions with minimal dissolution of the substrate, and also to introduce much higher solution Cd concentrations. The use of carbonate-containing solutions also allowed for a greater extent of overgrowth formation. Nonetheless, comparing the results on dolomite to those on calcite provided insight into the effects of structural dissimilarity between substrate and overgrowth on the growth process.

We discuss our current findings in the context of classical epitaxial film growth. Three general modes of epitaxial film growth have been characterized in the literature: (1) Volmer-Weber (3D islands), where interface energy is large, leading to the formation of nuclei on top of a bare substrate; (2) Frank-Van der Merwe (layer), where interface energy is low, and uniform layers are the dominant forms of growth on the surface; and the intermediate case (3) Stranski-Krastonov

(layer + 3D islands), where interface energy is comparable to island interaction energy, leading to the formation of nuclei on top of epitaxial film layers (e.g., Volmer and Weber, 1926; Stranski and Krastanov, 1939; Frank and Van Der Merwe, 1949; Brune and Kern, 1997; Benning and Waychunas, 2007). The mode of growth depends on the physical and chemical characteristics of the film and substrate. In particular, lattice misfit, which influences the balance between the cohesive forces in the growing solid and the adhesive forces between the solid and the substrate, is an important control.

The calcite and dolomite (104) surfaces are defined by rectangular lattices with dimensions *a* = 8.098 Å, *b* = 4.990 Å and *a* = 7.71 Å, *b* = 4.81 Å, respectively. The 'misfit' of otavite (*a* = 7.861 Å, *b* = 4.920 Å) on the dolomite substrate is given by:

$$misfit_{otavite\ on\ dolomite\ surface} = \frac{l_{otavite} - l_{dolomite}}{l_{dolomite}} \quad (12)$$

where l is a lattice cell parameter. The values for the misfit of otavite on dolomite in the *a* and *b* directions are 2.0% and 2.3 %, respectively, whereas those for otavite on calcite are -2.9% and -1.4%, respectively. Positive and negative values for misfit signify compressive and tensile stresses on the otavite film, respectively.

A similar approach was taken by Pimentel et al. (2013) to investigate the variation in the growth of calcite on dolomite and kutnahorite ($CaMn(CO_3)_2$) surfaces using AFM. The misfit values (Eq. 14) of calcite on dolomite (5.2% and 3.8% in *a* and *b*) and calcite on kutnahorite (3.3% and 2.3% in *a* and *b*) are higher than those in our experiments. Pimentel et al. (2013) observed Volmer-Weber growth mode for both substrates as might be expected due to the large strains. In general, the type of growth observed in our AFM experiments on both dolomite and calcite is consistent with the Stranski-Krastanov mode, wherein growth takes place initially in a layer by layer mode followed by the formation of islands that minimize strain in the overgrowth. This

mechanism was also demonstrated in the lateral force microscopy (LFM) studies of Cubillas and Higgins (2009) and Hay et al. (2003). Our results on calcite are consistent with those of Zachara et al. (1991) who described the Cd sorption process as resembling the formation of surface precipitates, and with the epitaxial layer spreading mechanism proposed by Chiarello and Sturchio (1994), Chiarello et al. (1997), and Astilleros et al. (2006). Because of differences in the extent of growth caused by limited Cd amounts and varying reaction times in our experiments, the growth modes that were observed in the AFM for dolomite (Fig. 6) may not reflect all possible growth modes for each experimental condition. We did not observe differences in the overgrowth formation process on calcite and dolomite that can be attributed to differences in substrate-film misfit between the two substrates.

The AFM images and XR data show that the process of Cd-carbonate overgrowth formation on calcite is similar to that on dolomite in the following ways. (1) The overgrowth started to form mostly at the step edge sites, with a phase signature in AFM images that was distinct from the substrate. The overgrowth grew laterally, leading to full coverage of the substrate or previously grown layers. (2) Nucleation of monolayer islands on top of previous overgrowth layers occurred on both substrates. In the case of dolomite, monolayer islands also formed on terraces. (3) The monolayer islands that are ~3 Å in height have a similar fan shape on both dolomite and calcite. (4) The overgrowth phases are similar in composition, as evidenced by similar *d*-spacings obtained from XR data. While the film vertical lattice spacing might be interpreted as due to a film with an apparent composition of about $Cd_{0.5}Ca_{0.5}CO_3$, this appears instead to be explained by the strain in the overgrowth that was caused by the substrate-film misfit. Specifically, we infer that the strain in the film (and not the composition) is most likely to have caused the increase in the *d*-spacing from the value that would be expected for an extremely Cd-rich solid solution (~2.95 Å). Evidence

of strain in otavite films was previously presented by Chiarello and Sturchio (1994) using specular XR. They observed compression in the vertical layer spacing of thin (~36.6 Å) otavite films.

4.4 Formation of "tall islands" on the dolomite surface

Tall islands 22 – 27 Å high were observed in previous Cd film growth studies on calcite, and were interpreted as ~8 layers of $CdCO_3$ precipitates (Perez-Garrido et al., 2007; Xu et al., 2014). We attempted to replicate these results, but the tall islands did not appear in any of our AFM images on calcite. However, we did observe the formation of tall islands in *in situ* experiments on dolomite under various conditions: (1) during monolayer growth of Cd-carbonate (Figs. 3C and 3E), wherein the tall islands comprise less than ~5% of the overgrowth in terms of surface coverage; (2) after flushing with water the dolomite surface that had been previously reacted with 50 µM $CdCl_2$ (Fig. EA14); and (3) during a 1-day *in situ* AFM experiment in which dolomite was reacted with DIW (not shown). Ex-situ XR data (Fig. EA15) and XRIM images (not shown) for a sample prepared as in case (2) (Fig. EA14), did not show any evidence that these tall islands were composed of oriented and crystalline $CdCO_3$, as was observed for otavite growth under all other conditions that were studied. In fact, the data showed no features associated with a thin-film Bragg peak (with an expected vertical width of ~$2\pi/25$Å = 0.25 $Å^{-1}$) within a range of vertical momentum transfers of 0.5 $Å^{-1}$ to 5 $Å^{-1}$ (i.e., for Bragg plane spacings of ~12 Å to ~1.3 Å, respectively) either in the specular signal (due to oriented growth) or in the background signals (e.g., due to growth of a randomly ordered material). This suggests that this tall island phase was either amorphous or had a different crystallographic orientation such that it did not appear in these specular XR measurements. Further, the presence of Cd in samples composed of tall islands only was not unambiguously confirmed with any of the X-ray techniques. Consequently, we were not able to

directly identify the composition or crystal structure of the tall islands, but we have included the tall islands as part of the range of overgrowths observed in this work (e.g., Fig. 6). Similar features that were 22 Å high were observed by Urosevic et al. (2012) during dolomite dissolution in pH-adjusted DIW. These features were interpreted as Mg-rich precipitates such as nesquehonite ($MgCO_3 \bullet 3H_2O$). This composition is consistent with the experimental conditions where the tall islands were observed by AFM in the present study, but does not explain the presence of tall islands in previous studies on calcite where no Mg-containing phase was present.

5. Conclusions

The present results provide a broad picture of interrelationships among solution saturation state, overgrowth morphology, and substrate characteristics that define the processes that control the formation of otavite films on dolomite and calcite. The combination of atomic force microscopy and synchrotron X-ray techniques allowed us to systematically examine the thermodynamic and kinetic controls on the incorporation of Cd in these films. We measured the amount of sorption and observed the internal structure of the overgrowth from a combination of *ex situ* X-ray reflectivity and X-ray fluorescence, and illustrated the morphology of this phase with *in situ* and *ex situ* AFM. We have shown that the rate of overgrowth formation is primarily controlled by the solution supersaturation and the surface step density of the dolomite substrate. The growth mechanism in our experiments is characterized by a Stranski-Krastanov growth mode, wherein growth ensues through both layer-by-layer and island formation mechanisms. We have experimentally determined rate constants and empirical coefficients that describe the kinetics of the uptake of Cd from rate equations that are based on the Gibbs free energy of the reaction, which in turn is dependent on the solution supersaturation. Direct comparison of XR and XRF

measurements revealed that the total Cd coverage measured by XRF was generally higher than that observed by XR, especially at larger film thicknesses, corresponding to the component of Cd-carbonate overgrowth that was oriented epitaxially to the dolomite substrate. The composition of this phase as inferred based on the film *d*-spacing obtained from XR is inconsistent with thermodynamic predictions and may reflect lattice strain in the overgrowth phase.

The use of the slowly dissolving dolomite substrate enabled experiments over a relatively large range of Cd concentrations, solution supersaturations and film thicknesses. Although this work focused on dolomite substrates and the experiments on calcite were limited, valuable comparisons could still be made. The process of Cd incorporation on dolomite was similar to that on calcite in a number of ways. Particularly, the overgrowths had similar vertical film layer spacings of ~3 Å and similar morphologies which ranged from monolayers growing at step edges to two-dimensional fan-shaped islands. The positive (compressive strain) and negative (tensile strain) misfits on dolomite and calcite substrates, respectively, did not cause significant differences in the growth behavior, except for the slightly smaller vertical layer spacing in the otavite film grown on calcite. This layer spacing was for a thin film only 3 layers thick; thick films on calcite that can be compared more directly to those on dolomite were not obtained in this study. These similarities indicate that the research findings may be generalized to other carbonate systems such as $MgCO_3$, $FeCO_3$ and $ZnCO_3$ of similar structures. A major difference is that in our experimental conditions, the growth of otavite on calcite appears to be self-limiting since it requires dissolution of calcite to provide the carbonate needed for growth of an otavite film.

Our new findings were also beneficial in providing new insight into the appearance of "tall islands" with typical heights of ~25 Å. Although we were unable to observe this phase on calcite substrates, we did observe their formation at the lowest Ca and CO_3 concentrations on dolomite.

Our structural observations suggest that this phase is not associated with the formation of a thick crystalline $CdCO_3$ phase. The precise nature of the tall-island phase is yet to be determined.

This work is of fundamental importance to models of carbonate geochemistry particularly in cases where metals such as Cd interact with and are incorporated into carbonate minerals. Further, another goal of this research was to use the fundamental data obtained on Cd-carbonate overgrowth behavior to provide insight into the likelihood that metal sequestration with carbonate minerals such as calcite and dolomite may occur in natural settings. The use of dolomite substrate allowed for an investigation of a wide range of solution Cd concentrations and for comparisons with observations on calcite in the literature. More specifically, these studies elucidated the role of dolomite as an amendment to remove Cd from contaminated soils. The Cd concentrations tested in the experiments of this study were higher than typical Cd concentrations in the environment, which are below the detection limits of the surface analytical methods. Hence, the findings would apply directly to heavily contaminated mine sites or electronic waste sites and by extrapolation to less contaminated sites.

6. Acknowledgments

The authors thank Richard Reeder for valuable suggestions on the experimental approach and Joanne Stubbs for beamline support at APS. This work was supported by the Geosciences Research Program of the Office of Basic Energy Sciences, U.S. Department of Energy (DOE), through contract number DE-AC02-06CH11357 to UChicago Argonne, LLC as operator of Argonne National Laboratory. X-ray-based measurements were performed at beamlines 13-BM-C and 13-ID-C (GeoSoilEnviroCARS), and 33-ID-D (X-ray Operations and Research) at the Advanced

Photon Source, Argonne National Laboratory. TheGeoSoilEnviroCARS facility is supported by NSF - Earth Sciences (EAR-1128799) and DOE-BES - Geosciences (DE-FG02-94ER14466).

7. References

Aagaard, P. and Helgeson, H. (1982) Thermodynamic and kinetic constraints on reaction rates among minerals and aqueous solutions: I. Theoretical considerations. *Am. J. Sci.* **282**, 237-285.

Agency for Toxic Substances and Disease Registry (ATSDR) (1997) Toxicological Profile for Cadmium. *Draft for Public Comment. Public Health Service,* U.S. Department of Health and Human Services, Atlanta, GA.

Ahmed, I., Crout, N. and Young, S. (2009) Kinetics of Cd sorption, desorption and fixation by calcite: a long-term radiotracer study. *Geochim. Cosmochim. Acta* **72**, 1498-1512.

Astilleros, J. Pina, C. Fernandez-Diaz, L., Prieto, M. and Putnis, A. (2006) Nanoscale phenomena during the growth of solid solutions of calcite (10-14) surfaces. *Chem. Geol.* **225**, 322-335.

Bar, G., Thomann, Y., Brandsch, R., and Cantow, H.J. (1997) Factors affecting the height and phase images in tapping mode Atomic Force Microscopy. Study of phase-separated polymer blends of poly(ethene-co-styrene) and poly(2,6-dimethyl-1,4-phenylene oxide). *Langmuir* **13**, 3807-3812.

Benning, L. and Waychunas, G. (2007) Nucleation, growth, and aggregation of mineral phases: mechanisms and kinetic controls, in *Kinetics of Water-Rock Interactions*, Springer Science+Business Media, LLC.

Brune, H. and Kern, K. (1997) Heteroepitaxial metal growth: the effects of strain. *Growth and Properties of Ultrathin Epitaxial Layers* **8**,149-206.

Callagon, E. B. R. (2016), High-resolution studies of cadmium uptake on carbonate surfaces: mechanisms, rates, and structures, PhD Thesis, University of Illinois, Chicago.

Callagon, E., Fenter, P., Nagy, K. and Sturchio, N. (2014) Incorporation of Pb at the calcite (104)-water interface. *Environ. Sci. Technol.* **48**, 9263-9269.

Chada, V., Hausner, D., Strongin, D., Rouff, A. and Reeder, R. (2005) Divalent Cd and Pb uptake on calcite {1014} cleavage faces: an XPS and AFM study. *J. Colloid Interf. Sci.* **288**, 350-360.

Chang, L. and Brice, W. (1971) Subsolidus phase relations in the system calcium carbonate-carmium carbonate. *Am. Mineral.* **56**, 338-341.

Chiarello, R. and Struchio, N. (1994) Epitaxial growth of otavite on calcite observed in situ by synchrotron X-ray scattering. *Geochim. Cosmochim. Acta* **58**, 5633-5638.

Chiarello, R., Sturchio, N., Grace, J., Geissbuhler, P., Sorensen, L., Cheng, L. and Xu, S. (1997) Otavite-calcite solid-solution formation at the calcite-water interface studied in situ by synchrotron X-ray scattering. *Geochim. Cosmochim. Acta* **61**, 1467-1474.

Chou, L., Garrels, R. and Wollast, R. (1989) Comparative study of the kinetics and mechanisms of dissolution of carbonate minerals. *Chem. Geol.* **78**, 269-282.

Cubillas, P. and Higgins, S. (2009) Friction characteristics of Cd-rich carbonate films on calcite surfaces: implications for compositional differentation at the nanometer scale. *Geochem. T.* **10**, 7.

Davis, J., Fuller, C. and Cook, A. (1987) A model for trace metal sorption processes at the calcite surface: adsorption of Cd^{2+} and subsequent solid solution formation. *Geochim. Cosmochim. Acta* **51**, 1477-1490.

Fenter, P. (2002) X-ray reflectivity as a probe of mineral-fluid interfaces: a user guide. *Rev. Mineral. Geochem.* **49**, 149-220.

Fenter, P., Cheng, L., Park, C., Zhang, Z. and Sturchio, N. C. (2003) Structure of the orthoclase (001)-and (010)-water interfaces by high-resolution X-ray reflectivity. *Geochim. Cosmochim. Acta* **67**, 4267-4275.

Fenter, P., Park, C., Zhang, Z. and Wang, S. (2006) Observation of subnanometre-high surface topography with X-ray reflection phase-contrast microscopy. *Nat. Phys.* **2**, 700-704.

Fenter, P., Lee, S.S., Park, C., Catalano, J.G., Zhang, Z. and Sturchio, N.C. (2010). Probing interfacial reactions with X-ray reflectivity and X-ray reflection interface microscopy: Influence of NaCl on the dissolution of orthoclase at pOH 2 and 85 C. *Geochim. Cosmochim. Acta* **74**, 3396-3411.

Frank, F. C. and Van der Merwe, J.H. (1949) One-dimensional dislocations. II. Misfitting monolayers and oriented overgrowth. In *Proceedings of the Royal Society of London A: Mathematical, Physical and Engineering Sciences* **198**, 216-225.

Gamsjager, H., Konigsberger, E. and Preis, W. (2000) Lippmann diagrams: theory and application to carbonate systems. *Aquat. Geochem.* 6: 119-132.

Glynn, P. and Reardon, E. (1990) Solid-solution aqueous-solution equilibria: thermodynamic theory and representation. *Am. J. Sci.* **290**, 164-201.

Glynn, P. (2000) Solid-solution solubilities and thermodynamics: sulfates, carbonates and halides. In *Rev. Mineral. Geochem.* **40**, 480-511.

Godt, J., Scheidig, F., Grosse-Siestrup, C., Esche, V., Branderburg, P., Reich, A. and Groneberg, D. (2006) The toxicity of cadmium and resulting hazards for human health. *J. Occup. Med. Toxicol.* **1**, 1-6.

Hay, M., Workman, R. and Maine, S. (2003) Mechanisms of metal ion sorption on calcite: composition mapping by lateral force microscopy. *Langmuir* **19**, 3727-3740.

International Agency for Research on Cancer (1993) Summaries & evaluations: cadmium and cadmium compounds (Group 1). Lyon, p. 119 (*IARC monographs on the evaluation of carcinogenic risks to humans*, 58; http://www.inchem.org/documents/iarc/vol58/mono58-2.html).

International Programme on Chemical Safety (1992) Cadmium. World Health Organization, Geneva, Switzerland (Environmental Health Criteria 134, http://www.inchem.org/documents/ehc/ehc/ehc134.htm).

Inskeep, W. and Bloom, P. (1985) An evaluation of rate equations for calcite precipitation kinetics at pCO_2 less than 0.01 atm and pH greater than 8. *Geochim. Cosmochim. Acta* **49**, 2165-2180.

Kocaoba, S. (2007) Comparison of Amberlite IR 120 and dolomite's performances for removal of heavy metals. *J. Hazard. Mater.* **147**, 488-496.

Kohler, S., Cubillas, P., Rodriguez-Blanco, Bauer, C. and Prieto, M. (2007) Removal of cadmium from wastewaters by aragonite shells and the influence of other divalent cations. *Environ. Sci. Technol.* **41**, 112-118.

Konigsberger, E., Hausner, R. and Gamsjager, H. (1991) Solid-solute phase equilibria in aqueous solution. V: The system $CdCO_3$-$CaCO_3$-CO_2-H_2O. *Geochim. Cosmochim. Acta* **55**, 3505-3514.

Laanait, N., Zhang, Z., Schlepütz, C.M., Vila-Comamala, J., Highland, M.J. and Fenter, P. (2014) Full-field X-ray reflection microscopy of epitaxial thin-films. *J. Synchrotron Radiat.* **21**, 1252-1261.

Laanait, N., Callagon, E. B. R., Zhang, Z., Sturchio, N. C., Lee, S. S., and Fenter, P. (2015) X-ray Driven Reaction Front Dynamics at Mineral-Aqueous Interfaces, *Science*, **349**(6254), 1330-1334.

Lasaga, A., Soler, J., Ganor, J., Burch, T. and Nagy, K. (1994) Chemical weathering rate laws and global geochemical cycles. *Geochim. Cosmochim. Acta* **58**, 2361-2386.

Lee, J., Choi, J. and Lee, K. (2005) Variations in heavy metal contamination of stream water and groundwater affected by an abandoned lead-zinc mine in Korea. *Environ. Geochem. Hlth* **27**, 237-257.

Lippmann, F. (1977) The solubility product of complex minerals, mixed crystals and three-layer clay minerals. *Neues Jahrbuch für Mineralogie* **130**, 243-263.

Lippmann, F. (1980) Phase diagrams depicting the aqueous solubility of binary mineral systems. *Neues Jahrbuch für Mineralogie* **139**, 1-25.

Martin-Garin, A., Van Capellen, P. and Charlet, L. (2003) Aqueous cadmium uptake by calcite: a stirred flow-through reactor study. *Geochim. Cosmochim. Acta* **67**, 2763-2774.

McBride, M. (1980) Chemisorption of Cd^{2+} on calcite surfaces. *Soil Sci. Soc. Am. J.* **44**, 26-28.

Mohammadi, M., Ghaemi, A., Torab-Mostaedi, M., Asadollahzadeh, M. and Hemmati, A. (2015) Adsorption of cadmium (II) and nickel (II) on dolomite powder. *Desalin. Water Treat.* **53**, 149-157.

Morse, J. and Arvidson, R. (2002) The dissolution kinetics of major sedimentary carbonate minerals. *Earth-Sci. Rev.* 58: 51-84.

Nancollas, G. and Reddy, M. (1971) The crystallization of calcium carbonate. *J. Colloid Interf. Sci.* **37**, 824-830.

National Institute for Occupational Safety and Health (2012) Workplace safety and health topics: cadmium, Centers for Disease Control and Prevention 1600 Clifton Road Atlanta, GA 30329-4027, USA, http://www.cdc.gov/niosh/topics/cadmium/

Office of Environmental Health Hazard Assessment (2007) Cadmium, http://www.oehha.ca.gov/public_info/pdf/cadmiumfacts.pdf

Papadopoulos, P. and Rowell, D. (1988) The reactions of cadmium with calcium carbonate surfaces. *J. Soil Sci.* **39**, 23-36.

Parkhurst, D. L. and Appelo, C. A. J. (2011) User's guide to PHREEQC (version 2) - a computer program for speciation, batch-reaction, one-dimensional transport, and inverse geochemical calculations, version 2.18.00, http://wwwbrr.cr.usgs.gov/projects/GWC_coupled/phreeqc/index.html

Pavlick, A. (1999) Solid solution/aqueous solution partitioning of cadmium to calcite: thermodynamics and transport, Ph.D. thesis, Student Scholar Archive paper 2534

Perez-Garrido, C., Fernandez-Diaz, L., Pina, C. M. and Prieto, M. (2007) In situ AFM observations of the interaction between calcite 1014 surfaces and Cd-bearing aqueous solutions. *Surf. Sci.* **601**, 5499-5509.

Pimentel, C., Pina, C.M. and Gnecco, E. (2013) Epitaxial growth of calcite crystals on dolomite and kutnahorite (104) surfaces. *Cryst. Growth Des.* **13**, 2557-2563.

Prieto, M., Putnis, A. and Fernandez-Diaz, L. (1993) Crystallization of solid solutions from aqueous solutions in a porous medium: zoning in $(Ba,Sr)CO_3$. *Geol. Mag.* **130**, 289-299.

Prieto, M., Fernandez-Gonzalez, A., Putnis, A., and Fernandez-Diaz, L. (1997) Nucleation, growth, and zoning phenomena in crystallizing $(Ba,Sr)CO_3$, $Ba(SO_4,CrO_4)$, $(Ba,Sr)SO_4$, and $(Cd,Ca)CO_3$ solid solutions from aqueous solutions. *Geochim. Cosmochim. Acta* **61**, 3383-3397.

Prieto, M., Cubillas, P. and Fernandez-Gonzalez, A. (2003) Uptake of dissolved Cd by biogenic and abiogenic aragonite: a comparison with sorption onto calcite. *Geochim. Cosmochim. Acta* **67**, 3859-3869.

Prieto, M. (2009) Thermodynamics of solid solution-aqueous solution systems. *Rev. Mineral. Geochem.* 70: 47-85.

Rao, K. S., Mohapatra, M., Anand, S. and Venkateswarlu, P. (2010) Review on cadmium removal from aqueous solutions. *Int. J Eng. Sci. Technol.* **2**, 81-103.

Reeder, R. (1996) Interaction of divalent cobalt, zinc, cadmium, and barium with the calcite surface during layer growth. *Geochim. Cosmochim. Acta* **60**, 1543-1552.

Rochayati, S., Verloo, M. and Du Laing, G. (2010) Availability of cadmium and zinc as affected by the use of reactive phosphate rock, lime, and chicken manure on an Indonesian acidic upland soil under field conditions. *Commun. Soil Sci. Plan.* 41: 1986-2003.

Robinson, I.K. (1986) Crystal truncation rods and surface roughness. *Phys. Rev. B* **33**, 3830.

Rock, P., Casey, W., McBeath, M. and Walling, E. (1994) A new method for determining Gibbs energies of formation of metal-carbonate solid solutions: 1. The $Ca_xCd_{1-x}CO_3$(s) system at 298 K and 1 bar. *Geochim. Cosmochim. Acta* **58**, 4281-4291.

Shannon, R.T. and Prewitt, C.T. (1969) Effective ionic radii in oxides and fluorides. *Acta Crystallog B - Stru.* **25**, 925-946.

Stipp, S., Hochella, M., Parks, G. and Leckie, J. (1992) Cd^{2+} uptake by calcite, solid-state diffusion, and the formation of solid-solution: interface processes observed with near-surface sensitive techniques (XPS, LEED, and AES). *Geochim. Cosmochim. Acta* **56**, 1941-1954.

Stranski, I.N. and Krastanov, L. (1939) Akademie der Wissenschaften und Literatur Mainz, Mathematisch-Naturwissenschaftliche Klasse IIb **146**, 797.

Tesoriero, A. and Pankow, J. (1996) Solid solution partitioning of Sr^{2+}, Ba^{2+}, and Cd^{2+} to calcite. *Geochim. Cosmochim. Acta* **60**, 1053-1063.

Urosevic, M., Rodrigues-Navaroo, C., Putnis, C., Cardell, C., Putnis, A. and Ruiz-Agudo, E. (2012) In situ nanoscale observations of the dissolution of (1014) dolomite cleavage surface, *Geochim. Cosmochim. Acta* **80**, 1-13.

van der Weijden, R., van der Weijden, C. and Comans, R.J. (1994) Sorption and sorption reversibility of Cd on calcite under simulated riverine, estuarine and marine conditions. *Mar. Chem.* **47**, 65-79.

Volmer, M. and Weber, A. (1926) Keimbildung in übersättigten Gebilden. *Z. Phys. Chem* **119**, 277-301.

Vondráčková, S., Hejcman, M., Tlustoš, P. and Száková, J. (2013) Effect of quick lime and dolomite application on mobility of elements (Cd, Zn, Pb, As, Fe, and Mn) in contaminated soils. *Pol. J. Environ. Stud.* **22**, 577-589.

World Health Organization (2010) Exposure to cadmium: a major public concern. Public Health and Environment, World Health Organization Document Production Services, Geneva, Switzerland (http://www.who.int/ipcs/features/cadmium.pdf)

Xu, M., Kovarik, L., Arey, B. W., Felmy, A. R., Rosso, K. M. and Kerisit, S. (2014) Kinetics and mechanisms of cadmium carbonate heteroepitaxial growth at the calcite 1014 surface. *Geochim. Cosmochim. Acta* **134**, 221-233.

Xu, M., Ilton, E. S., Engelhard, M. H., Oafoku, O., Felmy, A. R., Rosso, K. M., Kerisit, S. (2015) Heterogeneous growth of cadmium and cobalt carbonate phases at the calcite surface. *Chem. Geol.* **397**, 24-36.

Yavuz, O., Guzel, R., Aydin, F., Tegin, I. and Ziyadanogullari, R. (2007) Removal of cadmium and lead from aqueous solution by calcite. *Pol. J. Environ. Stud.* **16**, 467-471.

Zachara J. M., Cowan C.E. and Resch C.T. (1991) Sorption of divalent metals on calcite. *Geochim. Cosmochim. Acta* **55**, 1549–1562.

Zhang, J. and Reeder, R.J. (1999) Comparative compressibilities of calcite-structure carbonates: Deviations from empirical relations. *Am. Mineral.* **84**, 861-870.

Figures

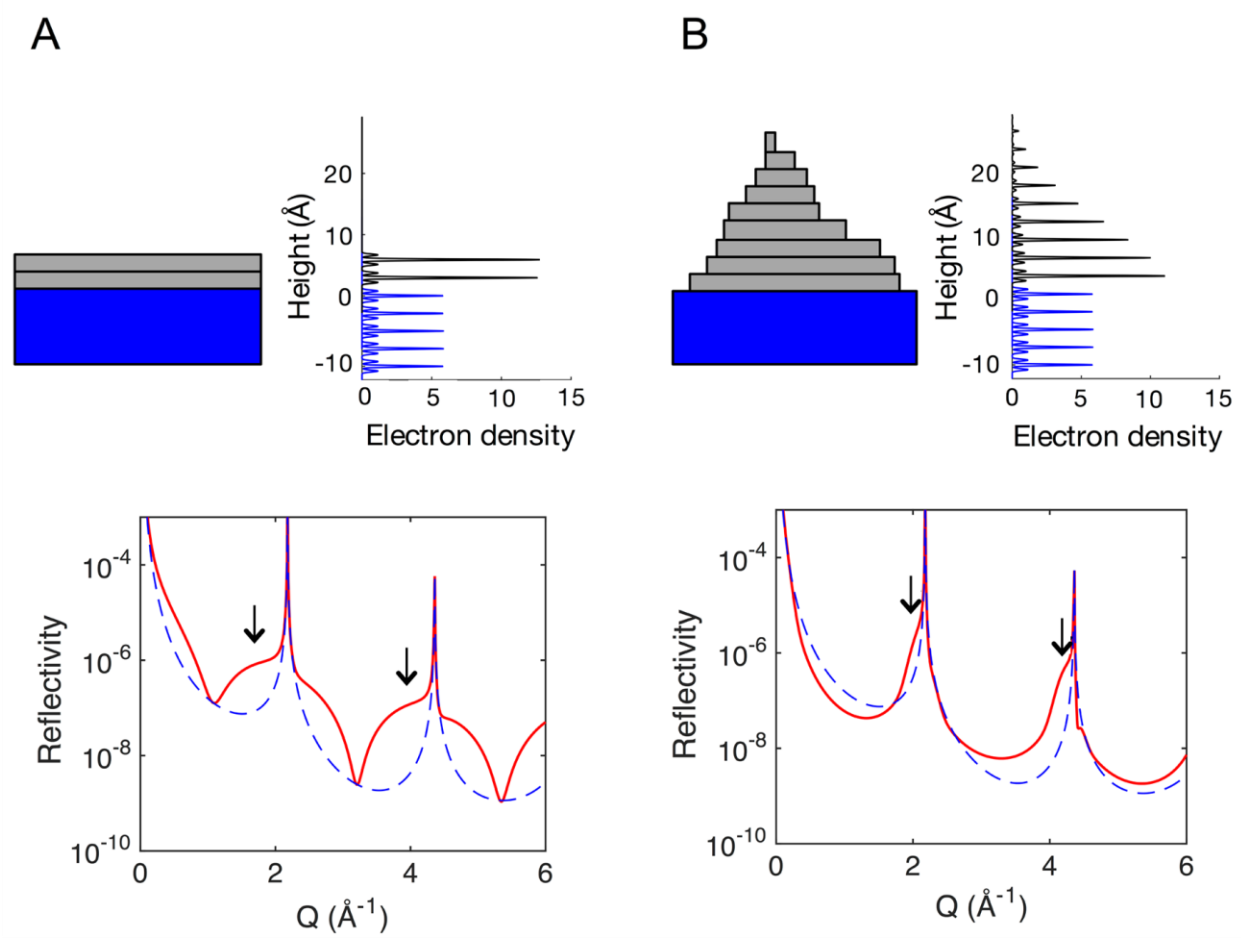

Figure 1. Model CTR calculations for a (A) smooth thin $CdCO_3$ film, i.e., 2 layers fully covering the substrate; and a (B) rough thick $CdCO_3$ film, i.e., ~9 partial layers with Cd occupancies rapidly decreasing away from the surface, using the model given in Eq. 6. In each case, a schematic of the film morphology and the corresponding electron density profile are given. The dolomite substrate and otavite film are represented in blue and grey, respectively. The calculations of reflectivity for the dolomite substrate (blue), and the combination of the substrate and the film (red) are shown. Total reflectivity (red) of (A) shows oscillations resulting from interference between the film layers, and broad (104) and (208) Bragg peaks (black arrows). For (B), the oscillations are not present, and Bragg peaks at Q corresponding to $CdCO_3$ (black arrows) are evident.

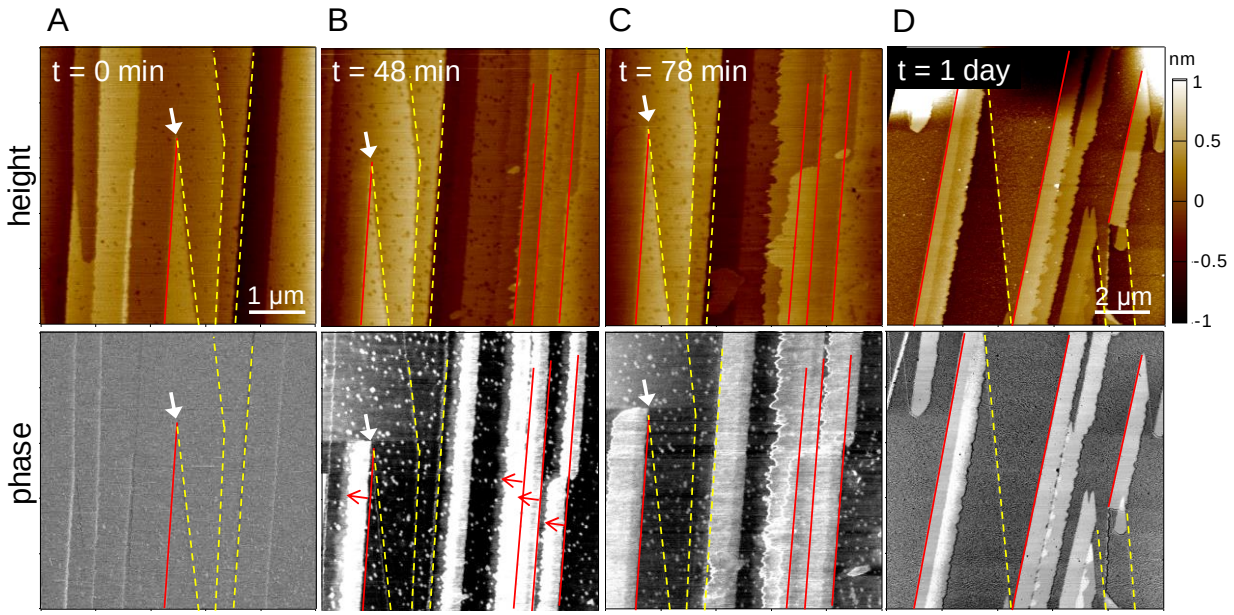

Figure 2. *In situ* and *ex situ* AFM images of growth on dolomite at low supersaturation (log $\beta_{max} \leq 1.0$): Height (top) and phase (bottom, in gray) images elucidate the evolution of the dolomite surface as the Cd-carbonate film (bright areas in phase images) grew at step edges, indicated by the red arrows. Features marked by white arrows in height and phase images in (A-C) are equivalent. Reaction times with Cd are indicated in each pair of images. Dissolution of dolomite is evident from the formation of pits on the surface in (A). Growth occurred on original dolomite step edges marked with solid red lines, but not on those marked with dashed yellow lines in (A-D). (A-C) *In situ* experiment with initial solution: [Cd] = 0.05 mM, [Ca] = [CO_3] = 0, wherein Ca and CO_3 is provided by the dissolution of dolomite substrate. (D) *Ex situ* surface after 1 day of reaction with an initial solution on a separate area: [Cd^{2+}] = 0.05 mM, [Ca^{2+}] = 0.212 [CO_3^{2-}] = 0.214 mM (XR-11); $\log \beta_{max}$ = 0.96.

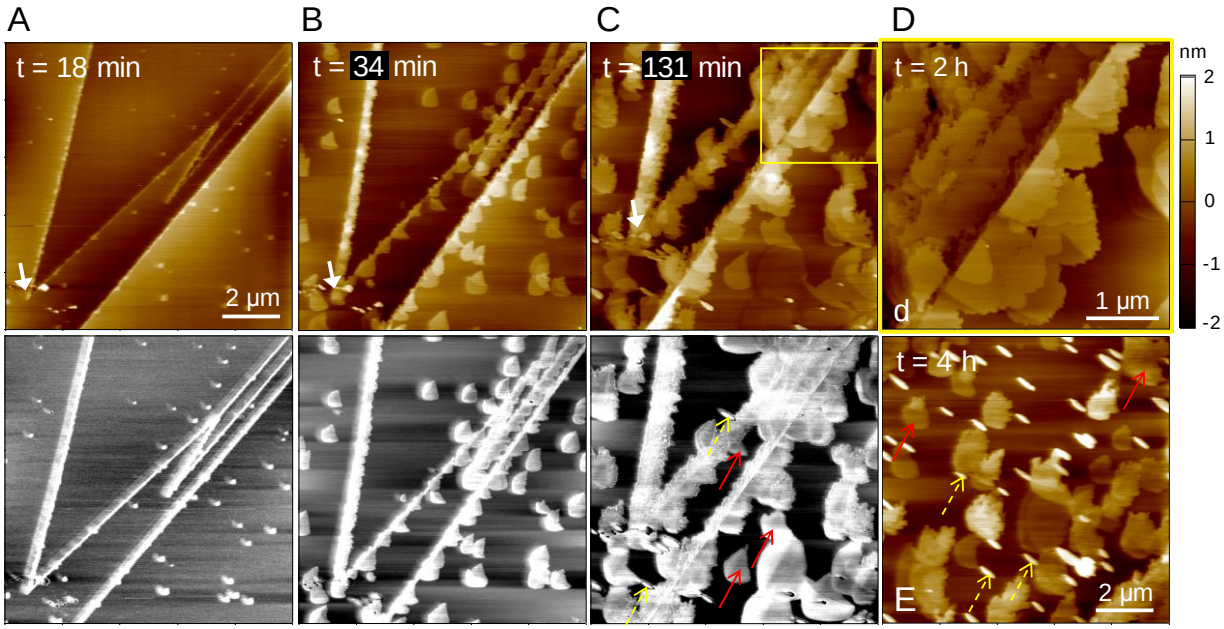

Figure 3. *In situ* AFM images of growth on dolomite at intermediate supersaturation (1.0 < log β_{max} < 2.0): Height and phase images show growth on dolomite originating from step edges (A, B, C, D), 3 Å monolayer islands (solid red arrows in C, phase, and E), and ~2.5 nm tall islands (dashed yellow arrows in C, phase, and E). Features marked by white arrows in height images in (A-C) are equivalent. (A-E) Images from a single sample reacted with solution containing [Cd^{2+}] = 0.203, [Ca^{2+}] = 0.201, [CO_3^{2-}] = 0.187 mM, and which has log β_{max}= 1.42. (A-C) Images of the same area on the sample. (E) Terrace area on the sample where tall islands are abundant. Some monolayer islands have an irregular shape (i.e., scalloped or ragged edges) exemplified in yellow box in (C) and shown in more detail in (D).

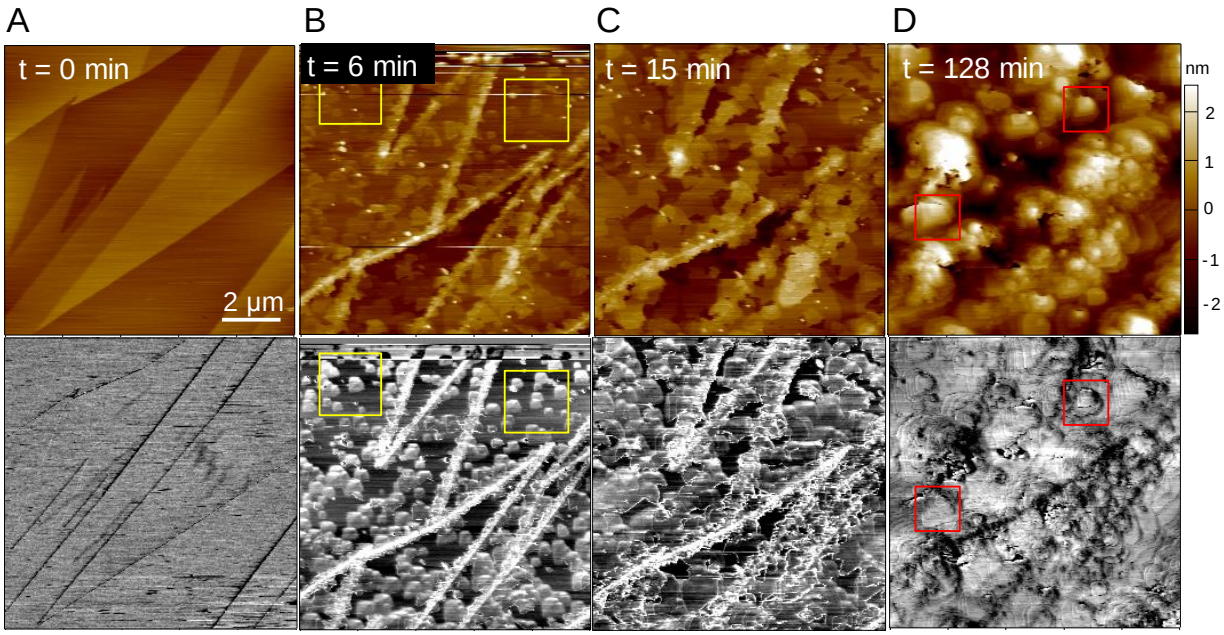

Figure 4. *In situ* AFM images of growth on dolomite at high supersaturation (log β_{max} > 2.0): Rapid nucleation and growth of 3 Å monolayer islands (yellow boxes in B, phase) are evident. Monolayer islands eventually covered the surface in (D), where features similar to those in Fig. EA6C (red boxes) are also evident. Initial solution: [Cd^{2+}] = 0.501, [Ca^{2+}] = 0.641, [CO_3^{2-}] = 0.545 mM; log β_{max}= 2.59.

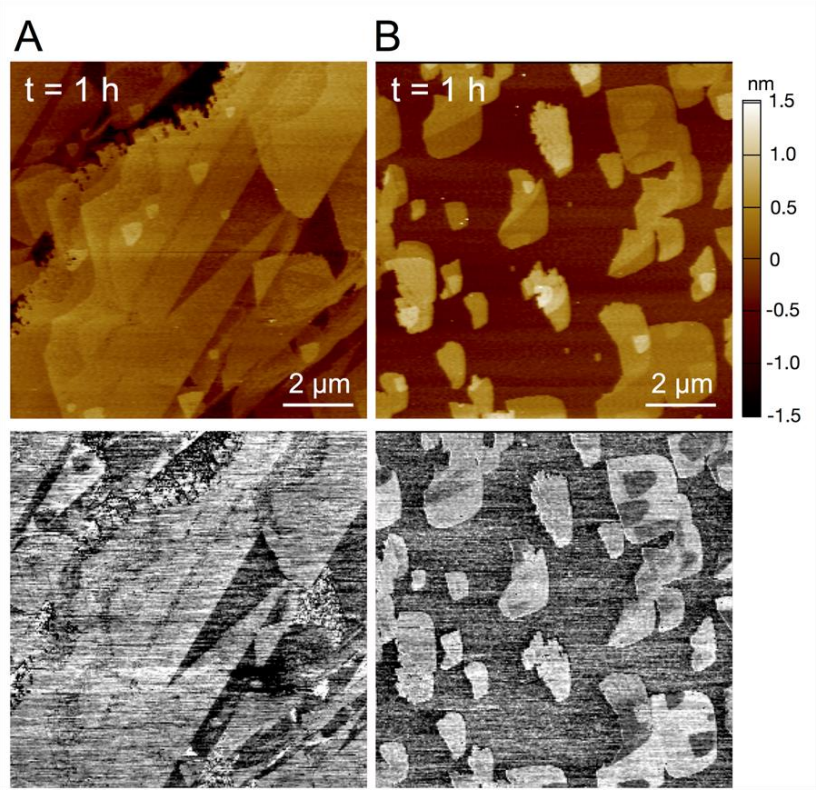

Figure 5. *Ex situ* AFM images for selected sample of dolomite reacted for 1 hour with solution at high supersaturation (log β_{max} > 2.0). Initial solution: [Cd] = 0.202 mM, [Ca] = [CO_3] = 0.75 mM, log β_{max} = 2.49. (A) and (B) are images at different areas of the same sample, illustrating the effect of substrate morphology on overgrowth coverage. The presence of substrate steps in (A) resulted in more growth as compared to (B). Overgrowth formation occurred through the formation of 3 Å monolayers on step edges and terraces.

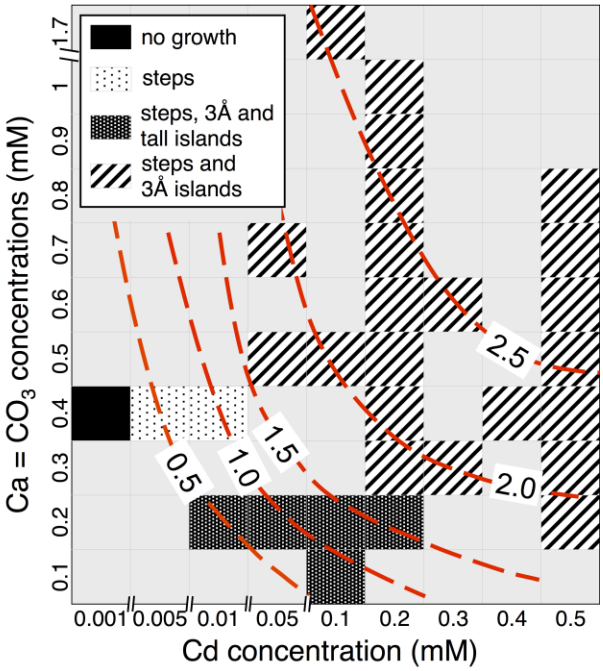

Figure 6. Summary of growth morphologies of Cd-carbonate on dolomite for various [Cd], [Ca], and [CO_3]. Observations for experiments in which [Ca] = [CO_3] are shown. Axes have variable scales, as indicated. Dashed curves indicate approximate equal $\log \beta_{max}$ curves of 0.5, 1.0, 1.5, 2.0 and 2.5.

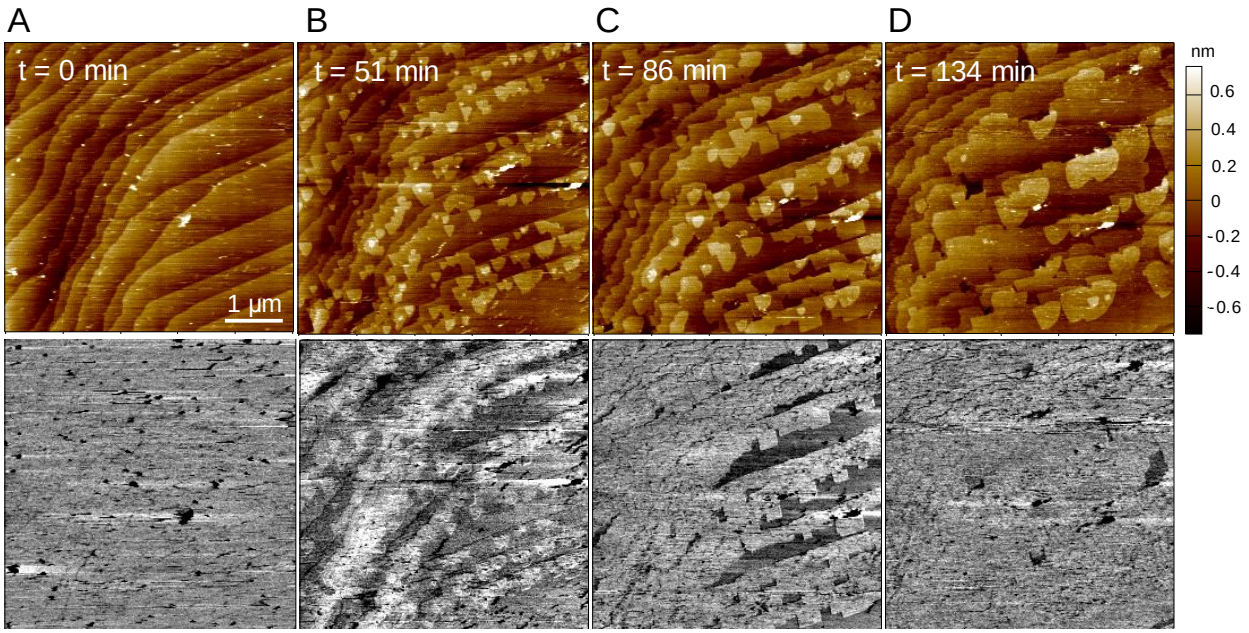

Figure 7. *In situ* AFM height and phase images of the same area on a calcite surface during reaction with 50 µM $CdCl_2$ solution as in Fig. EA7, but at longer reaction times. Growth occurred initially at step edges, and then continued by the nucleation and expansion of 3 Å islands. The monolayer islands coalesced and formed full layers, as shown in (D).

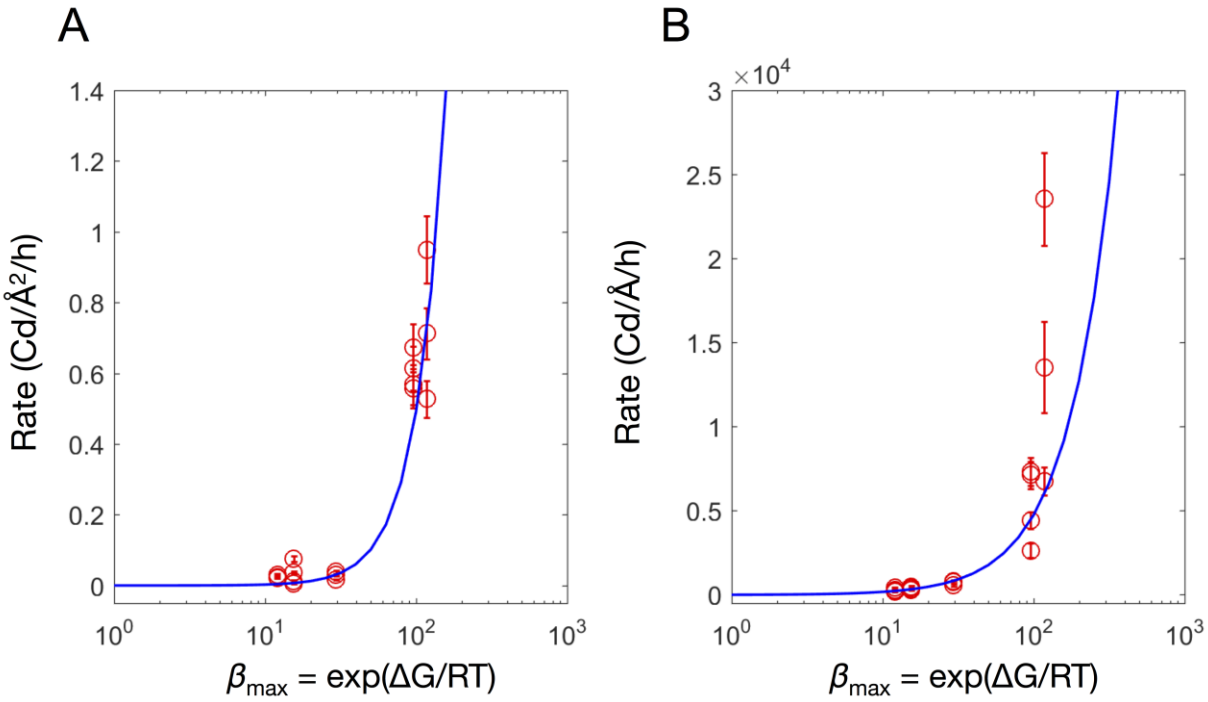

Figure 8. Variation of Cd uptake rate in (A) Cd/Å^2/h and (B) Cd/Å/h on dolomite from XRF measurements with β_{max} or $e^{\Delta G/RT}$. The best fits to Eq. 7 (blue curves) give rate coefficients, k, of (A) 1.31 × 10^{-5} Cd/Å^2/h and (B) 6.69 Cd/Å/h, and empirical constants, n, of (A) 2.29; and (B) 1.43. The quality of fit given by $\chi^2 = (1/N)\sum_i\left[\left(y_i - y_{i,calc}\right)/\sigma_i\right]^2$ and $R = (1/N)\sum_i\left|\left(y_i - y_{i,calc}\right)/y_i\right|$, where N, y_i, $y_{i,calc}$, and σ_i, are the number of data points, measured rate, best-fit rate, and measured uncertainty of the rate, respectively, and are (A) χ^2 = 28.1, R = 0.48, and (B) χ^2 = 7.6, R = 0.29. Rates for experiments at β_{max} < 1 are not plotted.

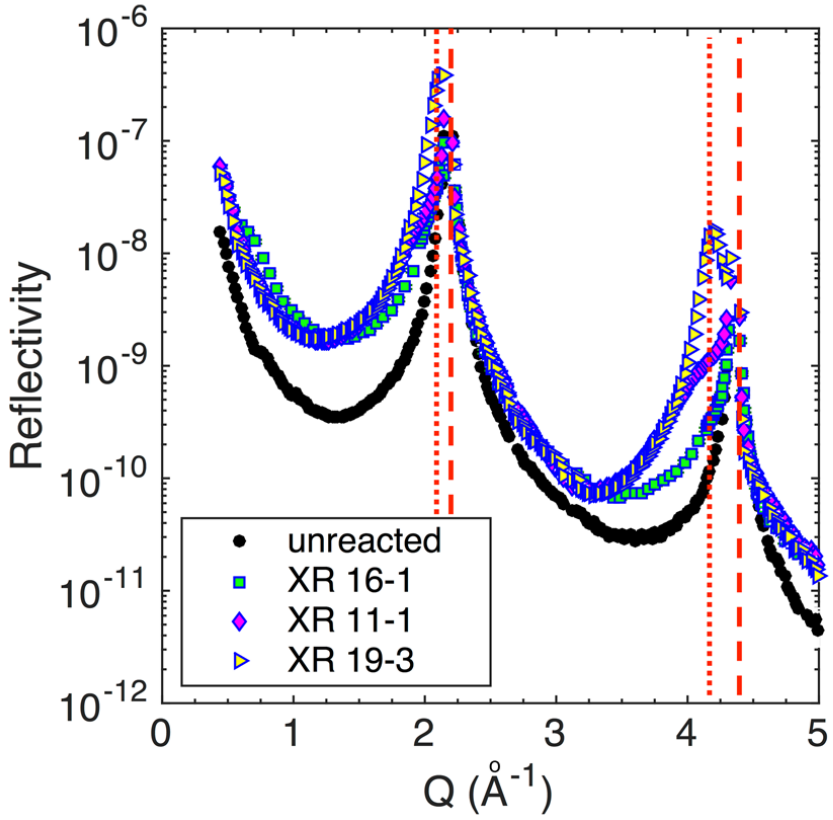

Figure 9. Representative X-ray reflectivity data (33-IDD) for three dolomite samples (sample numbers, as in Table 2, are given in the legend). Dashed and dotted red lines indicate *Q* values corresponding to the dolomite and film Bragg peaks, respectively. An overall increase in intensities is evident for CTRs of the Cd-reacted dolomite. Formation of Cd-rich carbonate phase on the Cd-reacted samples is seen as an overall increase in reflectivity, then as a 'shoulder' that evolves into a distinct Bragg peaks to the left of the dolomite Bragg peak. Initial solution saturation indices for Experiments XR-16, XR-11, and XR-19 are 1.48, 0.96, and 1.48, and the corresponding reaction times are 4, 24, and 24 h, respectively.

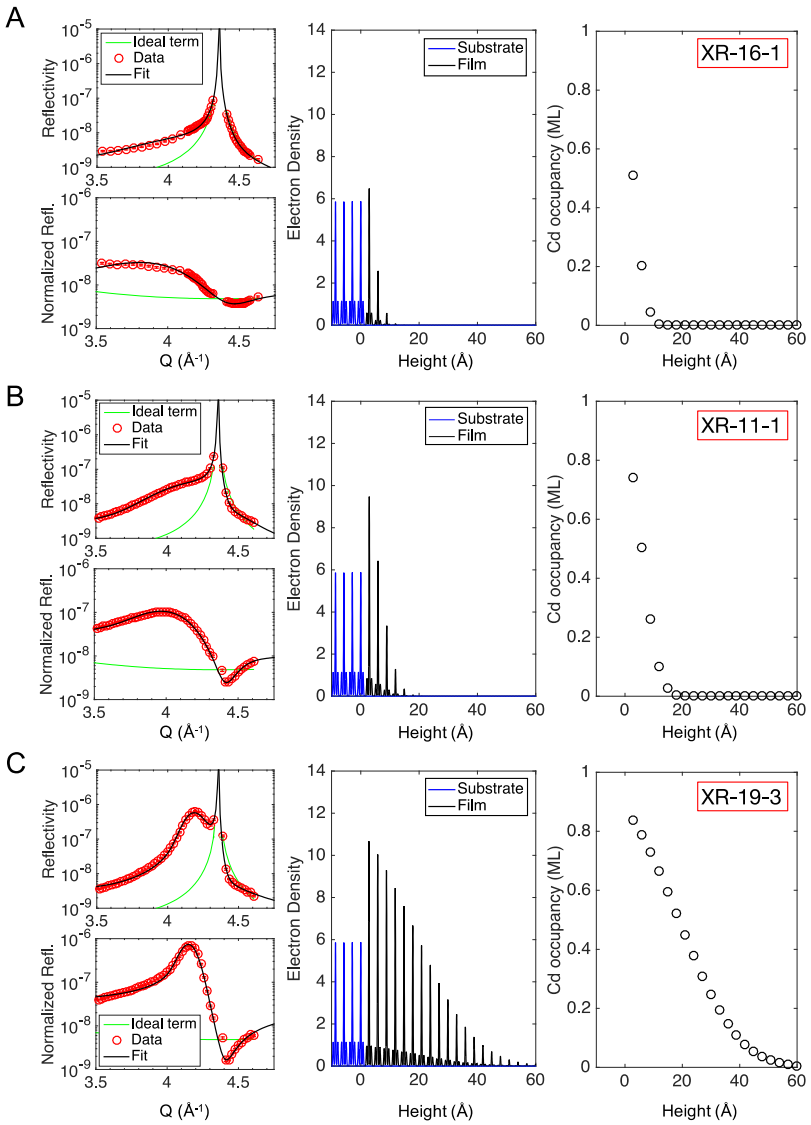

Figure 10. Analysis of XR data shown in Fig. 9 for growth on dolomite. Reflectivity signal (red circles, left panel) along with the same signal after normalization to the generic CTR shape, given by $R_{CTR} = 1/[Q\sin(Qd_{104}/2)]^2$ (Fenter, 2002) (black line is the fit to the data, green line is the signal from an ideally terminated dolomite surface). The corresponding electron density profile (middle) and Cd occupancy profile (right) for each respective sample are shown. Height = 0 Å at the substrate-film interface. The parameters as in Eq. 4 for the best-fit structure are given in Table EA5.

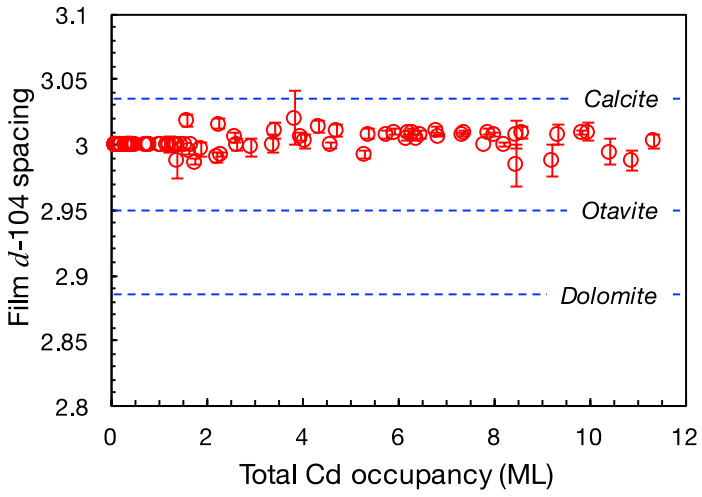

Figure 11. Film vertical layer spacing from analysis of XR data for growth of otavite on dolomite. Samples with low Cd occupancies ($\theta < \sim 1.5$ ML) and with film Bragg peaks that are not well-defined from the data have been assigned a fixed d_{104} of 3.0 Å, which is the average of the fitted d_{104} for the other samples, whose error bars are also indicated. The bulk d_{104} of calcite, otavite, and dolomite, are indicated for comparison. The average film vertical layer spacing has a value between those of calcite and otavite, indicating a solid solution.

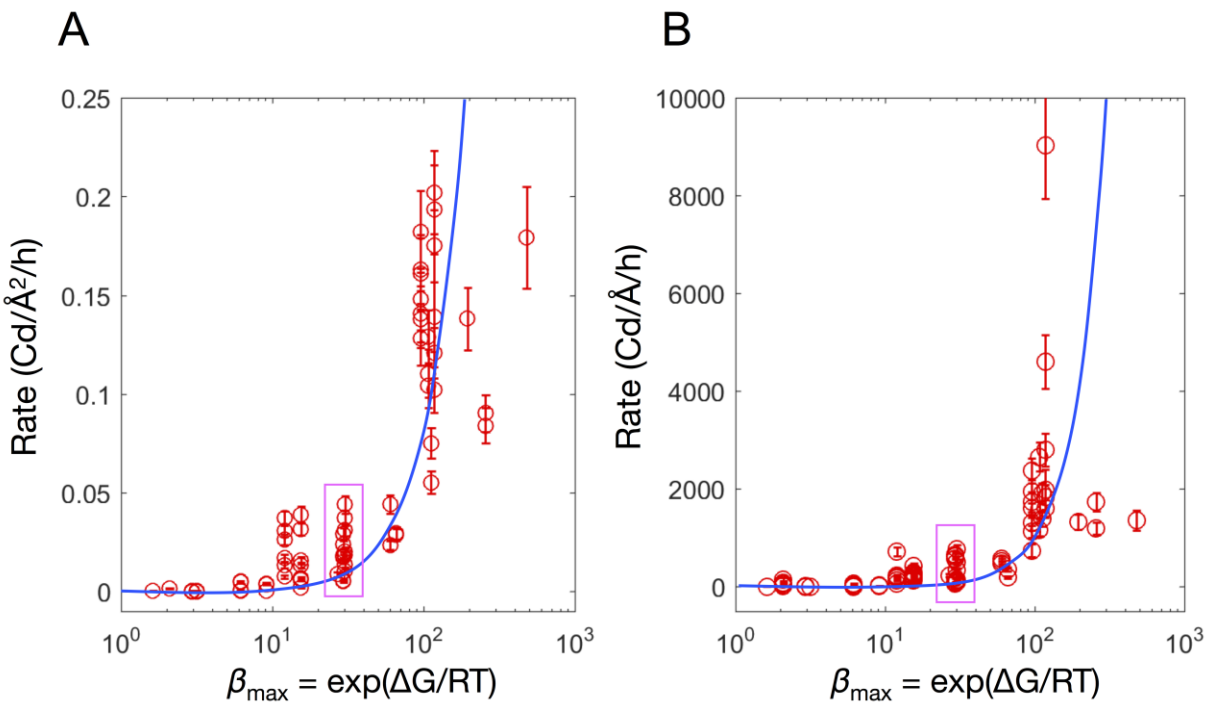

Figure 12. Variation of Cd uptake rate on dolomite in (A) Cd/Å^2/h and (B) Cd/Å/h from the analysis of the XR data as a function of β_{max} or $e^{\Delta G/RT}$. The best fits to Eq. 7 (blue curves) for experiments at 150 > β_{max} > 1 give rate constants, *k*, of (A) 2.27 × 10^{-5} Cd/Å^2/h and (B) 0.10 Cd/Å/h , and empirical coefficients, *n*, of (A) 1.77 and (B) 2.01. The quality of fit given by $\chi^2 = (1/N)\sum_i\left[\left(y_i - y_{i,calc}\right)/\sigma_i\right]^2$ and $R = (1/N)\sum_i\left|\left(y_i - y_{i,calc}\right)/y_i\right|$, where N, y_i, $y_{i,calc}$, and σ_i, are the number of data points, measured rate, best-fit rate, and measured uncertainty of the rate respectively, and are (A) χ^2 = 38.7, *R* = 0.60, and (B) χ^2 = 37.5, *R* = 0.62. Rates for experiments at β_{max} < 1 are not plotted. The change in growth rate with time (Fig. EA11) is considered using the data points outlined with a box in (A) and (B).

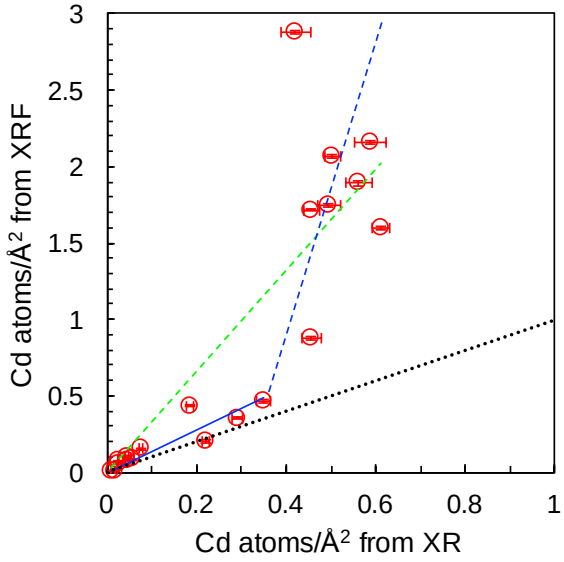

Figure 13. Comparison of Cd amounts grown on dolomite from XR and XRF measurements (Table EA7). The Cd occupancies in atoms/Å^2 were fitted with a line $y = ax$ with intercept set at 0. The parameters for the best-fit line are (solid blue) a = 1.38, R^2 = 0.82; (dashed green) a = 3.31, R^2 = 0.74. A dashed blue line indicates an approximate relationship between XR and XRF measurements at relatively higher Cd occupancies. A line with a slope of 1 (dotted black) is shown for reference.

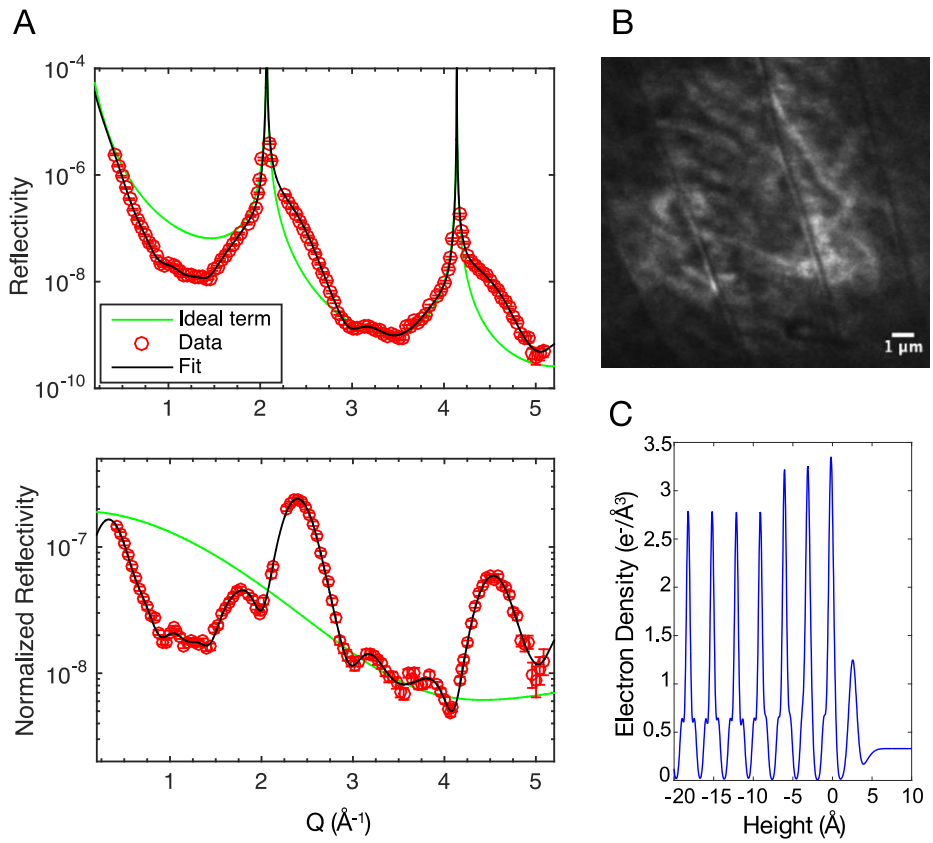

Figure 14. X-ray reflectivity and X-ray reflection interface microscopy data on Cd incorporation in calcite. (A) Reflectivity signal (top) of the calcite surface reacted with 10 µM Cd for 24 hours. The 'shoulder' to the right of the calcite Bragg peaks is the (104) Bragg peak from the Cd-rich phase (black line is the model fit to the data, and green line is the calculated reflectivity from an ideally terminated dolomite substrate ('ideal term'). The otavite Bragg peak at $Q \sim 2.4$ Å is distinct from that of calcite, as is most evident when seen in the normalized reflectivity after normalization by the generic CTR shape (given by $R_{CTR} = 1/[Q\sin(Qd_{104}/2)]^2$) and shown in panel A(bottom). (Fenter, 2002). (B) An *ex situ* XRIM image with a 40 second exposure at Q = 2.29 Å^{-1} (near the Bragg condition for the otavite (104) film Bragg peak). The brightness in the image is proportional to the local Cd concentration for a crystalline oriented otavite film. (C) Electron density structure for the best fit model in (A), showing an increase in electron density in the top three layers of calcite surface (here, the film-aqueous solution interface is at height = 0 Å) that is attributed to the incorporation of Cd, and the presence of layer containing adsorbed Cd.

Tables

Table 1. *In situ* and *ex situ* AFM experimental conditions

Experiment type	Initial solution concentrations (mM)			pH[a]	Saturation Indices			Reaction time (h)
	[Cd]	[Ca]	[CO_3]		SI[b] $CaCO_3$	SI[c] $CdCO_3$	$\log \beta_{max}$[d]	
ex situ	0.001	0.408	0.357	7.66	-1.21	-0.34	-0.28	93.75
ex situ	0.005	0.363	0.436	7.75	-1.09	0.54	0.55	93.75
ex situ	0.01	0.2	0.2	7.42	-1.99	0.21	0.21	17.4
ex situ	0.01	0.2	0.2	7.42	-1.99	0.21	0.21	120
ex situ	0.01	0.385	0.516	7.82	-0.93	0.97	0.98	93.75
in situ	0.052	0	0	5.61	-	-2.63	-	2
in situ	0.05	0.204	0.202	7.42	-1.98	0.91	0.91	4.12
ex situ	0.05	0.531	0.540	7.83	-0.77	1.68	1.68	1
ex situ	0.05	0.705	0.714	7.95	-0.43	1.88	1.88	1
ex situ	0.058	0.059	0.058	6.89	-3.57	-0.06	-0.06	1.23
ex situ	0.07	0.071	0.07	6.97	-3.33	0.17	0.17	1.2
ex situ	0.09	0.092	0.09	7.07	-3.01	0.49	0.49	1.17
ex situ	0.097	0.099	0.097	7.10	-2.91	0.58	0.58	1.13
in situ	0.102	0.206	0.207	7.43	-1.97	1.22	1.22	6
ex situ	0.1	0.537	0.552	7.84	-0.75	1.99	1.99	1
ex situ	0.1	1.780	1.698	8.29	0.59	2.71	2.71	1
ex situ	0.202	0.187	0.187	7.38	-2.10	1.42	1.42	1
in situ	0.203	0.201	0.187	7.38	-2.07	1.42	1.42	2.58
in situ	0.203	0.201	0.187	7.38	-2.07	1.42	1.42	6
ex situ	0.207	0.211	0.207	7.42	-1.97	1.51	1.51	1.1
in situ	0.208	0.265	0.21	7.43	-1.86	1.52	1.52	1.77
in situ	0.202	0.297	0.328	7.62	-1.44	1.88	1.88	3.18
ex situ	0.202	0.35	0.35	7.65	-1.32	1.92	1.92	1
ex situ	0.202	0.45	0.45	7.75	-1.01	2.12	2.12	1
ex situ	0.202	0.55	0.55	7.83	-0.76	2.27	2.27	1
ex situ	0.202	0.65	0.65	7.90	-0.56	2.39	2.39	1
ex situ	0.202	0.75	0.75	7.96	-0.39	2.49	2.49	1
ex situ	0.202	0.85	0.85	8.01	-0.24	2.58	2.58	1
ex situ	0.202	0.95	0.95	8.06	-0.11	2.65	2.65	1
ex situ	0.3	0.306	0.3	7.58	-1.52	1.95	1.95	1.07
ex situ	0.3	0.544	0.52	7.81	-0.83	2.37	2.37	1
ex situ	0.4	0.408	0.4	7.69	-1.17	2.29	2.29	1.03
ex situ	0.5	0.351	0.353	7.64	-1.35	2.27	2.27	1
ex situ	0.5	0.51	0.5	7.78	-0.91	2.53	2.53	1
ex situ	0.5	0.535	0.615	7.87	-0.72	2.70	2.70	1
ex situ	0.5	0.56	0.52	7.80	-0.84	2.56	2.56	1
ex situ	0.5	0.565	0.52	7.80	-0.84	2.56	2.56	1
ex situ	0.5	0.567	0.544	7.82	-0.80	2.60	2.60	1
in situ	0.501	0.641	0.545	7.82	-0.75	2.59	2.59	2.82
ex situ	0.5	0.76	0.738	7.94	-0.44	2.82	2.82	1
ex situ	0.5	0.764	0.782	7.96	-0.39	2.86	2.86	1

[a] calculated pH
[b] $\log IAP/K_{sp}$ as in Eq. 1
[c] $\log IAP/K_{sp}$ as in Eq. 2
[d] as in Eq. 3

Table 2. *Ex situ* XR and XRF experimental conditions

Sample number	Initial solution concentrations (mM)			pH[a]	Saturation Indices			Reaction time (h)	Cd mole fraction[e]
	[Cd]	[Ca]	[CO_3]		SI[b] $CaCO_3$	SI[c] $CdCO_3$	$\log \beta_{max}$[d]		
XR-1	0	1	0.2	7.40	-1.37	-	-	63.12	-
XR-2	0.001	0.4	0.4	7.71	-1.12	-0.24	-0.19	126.57	0.88
XR-3	0.001	0.999	0.2	7.40	-1.37	-0.91	-0.78	63.20	0.74
XR-4	0.001	0.999	0.2	7.40	-1.37	-0.91	-0.78	129.50	0.74
XR-5*	0.005	0.4	0.4	7.71	-1.12	0.46	0.47	71.53	0.975
XR-6	0.005	0.429	0.417	7.73	-1.06	0.49	0.50	100	0.975
XR-7	0.005	0.4	0.4	7.71	-1.12	0.46	0.47	126.45	0.975
XR-8	0.01	0.2	0.2	7.42	-1.99	0.21	0.21	71.57	>0.99
XR-9*	0.01	0.449	0.417	7.73	-1.05	0.79	0.79	100	0.985
XR-10	0.01	1	1	8.09	-0.02	1.42	1.43	124.67	0.965
XR-11*	0.05	0.211	0.214	7.44	-1.92	0.96	0.96	24	>0.99
XR-12	0.05	0.95	0.2	7.40	-1.40	0.78	0.79	4.53	>0.99
XR-13	0.1	0.2	0.2	7.41	-2.01	1.19	1.19	11.68	>0.99
XR-14	0.1	0.9	0.2	7.40	-1.42	1.08	1.08	3.32	>0.99
XR-15	0.2	0.05	0.05	6.82	-3.79	0.32	0.32	14.20	>0.99
XR-16*	0.2	0.211	0.202	7.41	-1.99	1.48	1.48	4	>0.99
XR-17	0.2	0.2	0.2	7.41	-2.02	1.47	1.47	12.00	>0.99
XR-18	0.2	0.2	0.2	7.41	-2.02	1.47	1.47	12.07	>0.99
XR-19*	0.2	0.211	0.202	7.41	-1.99	1.48	1.48	24	>0.99
XR-20	0.2	0.2	0.2	7.41	-2.02	1.47	1.47	46.50	>0.99
XR-21*	0.2	0.429	0.417	7.72	-1.09	2.05	2.05	1	>0.99
XR-22	0.25	0.75	0.2	7.40	-1.50	1.48	1.48	3.25	>0.99
XR-23	0.2	1	1	8.08	-0.05	2.68	2.68	3.00	>0.99
XR-24	0.4	0.4	0.4	7.69	-1.18	2.29	2.29	3.35	>0.99
XR-25	0.5	0.2	0.2	7.40	-2.05	1.82	1.82	11.70	>0.99
XR-26*	0.5	0.438	0.424	7.71	-1.11	2.41	2.41	1	>0.99
XR-27	0.5	0.5	0.2	7.40	-1.68	1.78	1.78	3.15	>0.99
XR-28	0.8	0.2	0.2	7.39	-2.08	1.98	1.98	3.08	>0.99
XR-29	0.9	0.1	0.2	7.39	-2.38	2.03	2.03	3.08	>0.99
XR-30	1	0	0.2	7.39	-	2.07	-	3.03	1

[a]calculated pH

[b]$\log \frac{IAP}{K_{sp}}$ as in Eq. 1

[c]$\log \frac{IAP}{K_{sp}}$ as in Eq. 2

[d]as in Eq. 3

[e] calculated mole fraction, *X*, of Cd in $(Cd_x,Ca_{1-x})CO_3$ solid solution at maximum supersaturation, β_{max}.

*AFM images were collected for these samples

Table 3. *In situ* and *ex situ* AFM experiments on calcite

Experiment type	Initial [Cd] (μM)	Reaction time (h)[a]	Number of replicates [b]
in situ	50	2	7
ex situ	50	3.5	1
in situ	10	5	1
ex situ	10	3	2
in situ	5	1.5	2
ex situ	1	3	1

[a]Maximum reaction time

[b]Number of replicates for the same experiment type and initial [Cd]

Table 4. Details of AFM experiments using method of Xu et al. (2014)

Experiment type	Volume of DIW (mL) [a]	Reaction time with DIW (min)[b]	Volume of 1 mM Cd added (μL)	Final [Cd^{2+}] (μM)	Reaction time with Cd solution (min)
in situ	2.5	30	80[c]	2	285
ex situ	1.5	30	3	2	120
ex situ	3	40	10	5	135
ex situ	1.5	30	6	5	155
ex situ	3	40	30	15	90
ex situ	2.5	15	60	20	53
ex situ	2.5	50	60	20	105
ex situ	1.5	30	24	20	175
in situ	2.5	30	80	30	270
ex situ	3	40	100	40	120
ex situ	1.5	30	60	50	200

[a]volume of DIW pre-reacted with calcite before addition of Cd

[b]reaction time of calcite with DIW before addition of Cd

[c]concentrated Cd solution is 50 μM instead of 1 mM for this experiment